Effect of substrate cooling and droplet shape and composition on the droplet evaporation and the deposition of particles

by

Vahid Bazargan

M.A.Sc., Mechanical Engineering, The University of British Columbia, 2008

B.Sc., Mechanical Engineering, Sharif University of Technology, 2006

B.Sc., Chemical & Petroleum Engineering, Sharif University of Technology, 2006

A THESIS SUBMITTED IN PARTIAL FULFILLMENT
OF THE REQUIREMENTS FOR THE DEGREE OF

Doctor of Philosophy

in

THE FACULTY OF GRADUATE AND POSTDOCTORAL STUDIES

(Mechanical Engineering)

The University Of British Columbia

(Vancouver)

March 2014

Abstract

Sessile droplets are liquid droplets resting on a flat substrate. During the evaporation of small sessile droplets, the contact line of the droplet undergoes two different stages: pinned stage with fixed contact area and de-pinned stage with fixed contact angle. An evaporation with a pinned contact line produces a flow inside the droplet toward the contact line. This flow carries particles and deposits them near the contact line. This causes the commonly observed "coffee-ring" phenomenon. This thesis provides a study of the evaporation process and the evaporation-induced flow of sessile droplet and brings insights into the deposition of particles from colloidal suspensions.

Here we first study the evaporation of small sessile droplets and discuss the importance of the thermal conductivity of the substrate on the evaporation process. We show how current evaporation models produce a significant error for droplet sizes below 500 μm. Our model includes thermal effects, in particular, it includes the thermal conductivity of the substrate that provides heat to the droplet to balance the latent heat of evaporation. It considers the whole time of evaporation with the pinned and the de-pinned stages by defining a virtual movement of the contact line that is related to the evolution of the contact angle and is based on experimental results. Our model is in agreement with experimental results for droplets smaller than 500 μm with an error below 2%.

Furthermore, we study the evaporation of line droplets with finite sizes and discuss the complex behavior of the contact lines during evaporation. We apply an energy formulation and show that the contact line starts receding from the two ends of line droplets with a contact angle above the receding contact angle of spherical droplets. And then we show the evaporation-induced flow inside the line droplets.

Finally, we discuss the behavior of the contact line under the presence of surfactant and discuss the Marangoni flow effects on the deposition of the particles. We show that the thermal Marangoni effect affects the amount of the particles deposited near the contact line, where a lower substrate temperature corresponds to a larger amount of particles depositing near the contact line.

Preface

This thesis is original, independent work by the author, Vahid Bazargan. This work was supported by NSERC through the Strategic Projects Grant program and the Discovery Grant program, The University of British Columbia through the Four Year Fellowship program, and the Howard Webster Foundation.

The experimental setup in Chapter 3 was designed and built primarily by myself, except for the temperature control system with a Peltier element in Section 3.2.2 that I used a code written by Simon Beyer and for the Graphical User Interface code in Section 3.2.1 that was written by Eton Leun as part of his EECE 496 course project. A licensed copy of FLOW-3D software was used for numerical simulation. The numerical model in Section 3.3 could not have been completed without the useful suggestions of Dan Milano.

A version of Chapter 4 is submitted for publication. I performed all parts of the research and I wrote the manuscript.

This work in Chapter 5 was carried out in conjunction with Charles Rabideau. He solved the energy equation for the line droplets in Section 5.2.1. A version of this chapter is submitted for publication. I am responsible for all major areas of concept formation and analysis, as well as the majority of manuscript composition.

A version of Chapter 6 is in preparation to be submitted for publication. I am responsible for conducting all parts of the research and preparing the manuscript.

The entire manuscript was prepared using the LaTeXpackage.

Table of Contents

List of Tables

List of Figures

Acknowledgments

This thesis, as with everything I have achieved in my life, would not have been possible without the encouragement, help and support of many people. My first debt of gratitude is to my supervisor Prof. Boris Stoeber for his ongoing support, generous encouragement and sound instruction. I can think of no other way in which I could have spent my student life that would have brought such satisfaction as working with him. I count myself incredibly fortunate.

I thank The University of British Columbia for support via the Four Year Fellowship program and the Howard Webster Foundation for support via R. Howard Webster Fellowships which has afforded me time to focus on this research. I also thank National Science and Engineering Research Council for supporting this work through the Strategic Projects Grant and the Discovery Grant programs.

I would like to thank Prof. Konrad Walus, Prof. Karen Cheung, Prof. Hongshen Ma and Prof. Mu Chiao for sharing their lab equipment, and for being generous with their time and knowledge. I also thank Prof. Savvas Hatzikiriakos and Prof. Dana Grecov for their comments on sections of this thesis. And a special thanks to my good friend and roommate Charles Rabideau for his help and detailed comments on chapter five.

I owe a great debt to my friends for their encouragement and help. I would like to thank especially my wonderful friends at Green College, one of the best places in the world and a place where I have encountered beautiful ideas and friendship. I would also like to thank Green College principal, Prof. Mark Vessey who brightened my day on many occasions with his helpful encouragement and wonderful speeches.

Finally, I would like to thank my Dad and my Mom for their support and their pa-

tience during my prolonged absence, and my brothers, Hamid and Mohammad. I would like to acknowledge my grandmother here for her incredible help while my mother brought up triplets. My grandmother passed away while I was writing this thesis. My heartfelt gratitude goes to her for her kindness and her patience, and for being relentless in seeking the best for us.

Dedication

To Mohammad Jahanara

Chapter 1

Introduction

1.1 Preliminary remarks

Technologies of the deposition of micro and nano particles from their suspensions has gained great scientific interest in recent years. The small size of these particles makes them effectively a bridge between bulk materials and atomic or molecular structures. Several methods have been proposed for structured deposition of micro and nano particles including gas flow, magnetic alignment, electrospray, quasi-2D nematic phase alignment, and electro spinning for different applications [2]. However the scalability of these methods for the precised placing of particles over large areas is still a challenge.

One of the most conventional ways to achieve a desired pattern of coating or placement of micro and nano particles on a large surface has been the controlled deposition of these particles from suspensions [3–8]. That is mainly owing to the fact that is relatively easy to achieve stable suspensions of micro and nano particles because Brownian motion and surface forces are strong enough to overcome differences in density. To achieve this goal, a technology for the systematic deposition of micro and nano particles from their suspending fluid is required. Sharma et al. [3, 9] showed that the controlled evaporation of the droplets containing nano particles lead to the precise placement of these particles with a precision on the order of a few nano meters. They generated lines of droplets in rectangular polar regions previously generated on a substrate. They showed that by pinning the line

droplet contact line to the polar pattern edges, a flow is generated during the evaporation that carries the nano particles toward the edges and places them uniformly onto the substrate. Dugas et al. [10] used the droplets of DNA solutions to form homogeneous oligoprobe spot deposition. They used a mixture of surfactants in the initial solution to control the behavior of the droplet shape during evaporation and to achieve the desired internal flow inside the droplet during evaporation. This flow generated during the evaporation of droplets was used by many researchers in various applications [11–15]. Therefore, investigating the evaporation of droplets and studying the internal flow during evaporation will be a major contribution to the understanding of this problem and can lead to many applications for particle deposition that were never possible before.

1.2 Sessile droplets

Sessile droplets are liquid droplets resting on a substrate in still air. They are not connected to or suspended from any fluid stream. The surface of the droplets is bounded by a gas phase that can usually be the atmospheric air. For droplets with a radius smaller than 1 mm, the effect of gravity is negligible and the shape of the droplet is defined by the surface tension that tends to make a spherical cap shape, as shown in Figure 1.1. The contact angle of the droplet is defined by the balance of the interfacial forces, i.e. fluid-gas (σ_{FG}), substrate-gas (σ_{SG}) and substrate-fluid (σ_{SF}).

Here we study the sessile droplets resting on a flat substrate that is indiffusible to the liquid. While there is no diffusion through the substrate, depending on the condition of the gas phase, a mass transfer between these the fluid and gas phases may occur that causes loss (evaporation) or accumulation (condensation) of the droplet volume. At room temperature, if the ratio of liquid vapor pressure in air to the saturated vapor pressure (known as “relative humidity” if the liquid is water) is less than 1, the number of liquid molecules leaving the surface of the droplet and diffusing into the ambient air is greater than the number of the vapor molecules diffusing into the droplet. This net transfer of liquid molecules to the air causes the loss of liquid volume. Accordingly, the evaporation process follows these two separate steps:

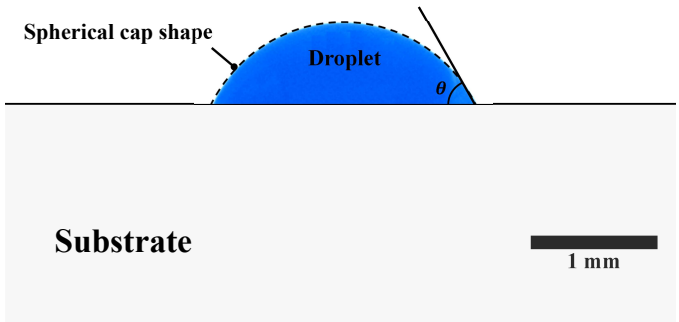

Figure 1.1: A water droplet with a radius of 1 mm resting on a glass substrate. The surface of the droplet takes on a spherical cap shape. The contact angle θ is defined by the balance of the interfacial forces.

1. Kinetics: where the liquid molecule at the fluid-gas interface receives the enthalpy of evaporation (a.k.a latent heat of evaporation), and transforms to a vapor molecule at the surface,

2. Diffusion: where the vapor molecule at the surface leaves the surface and goes to the ambient air.

The evaporation happens after the completion of these two steps. If one process is much slower than the other, it controls the evaporation process. Hence the evaporation can be classified to two different types: *Kinetically controlled evaporation*: where the kinetic transformation happens at a slower rate than the diffusion, and *Diffusion-controlled evaporation*: where the diffusive relaxation of the saturated vapor layer immediately above the drop defines the rate limiting step. In the former case, the evaporation is uniform over the surface, while in the later case, as will be shown in Chapter 2, the evaporation is strongly enhanced near the edge of the droplet.

For a small water droplet with a radius less than 1 mm (as shown in Figure 1.1), the time for the diffusion process at the surface of the droplet scales with $\sim R^2/D$, where R is the radius of the droplet D is the vapor diffusivity in air (26.1 mm^2/s). The time for the kinetic process, τ_k, is the water molecule transformation time scale and can be calculated from the Hertz-Knudsen equation [16]. For water molecules

at room temperature ($\sim 24°$C), τ_k is in the order of 10^{-10} s which is much faster than the diffusion process (~ 1 s). Thus, the assumption of the diffusion-controlled evaporation is justified.

The enhanced evaporation rate of sessile droplets with diffusion-controlled evaporation generated a non-uniform evaporation flux at the surface. This causes an internal flow inside the droplet. The details of this flow will be studied in the next chapter in Section 2.3. During evaporation of colloidal suspensions, this flow carries micro and nano particles and eventually deposits them on the substrate. Hence, understanding the evaporation-induced flow during evaporation along with the droplet shape during evaporation is a key part in understanding the deposition of colloidal suspensions.

1.3 Research objectives

The aim of this study is to investigate the diffusion controlled evaporation in small sessile droplets in the order of few hundred microns in diameter. The main parameters being particularly effective on the evaporation process of such small droplets was the main focus on our study. This is a key point in understanding the deposition of the particles along with the understanding of the shape of the droplet during evaporation. This objective will be achieved by solving the following three sub-problems:

1. We first review the current studies on the evaporation of pure liquids on a flat substrate and study the models that have so far been used to calculate the diffusion-controlled evaporation at the surface. We particularly show the strong influence of the substrate cooling on the evaporation of small droplets that seems to be missing in the previous studies.

2. The study of liquid line droplets generated by inkjet micro patterning will be the next goal. This particularly will be useful for the growing area of inkjet printing technology. We study the behavior of line droplets with finite aspect ratio and will discuss the evaporation time as well as the internal flow during the evaporation. The internal flow produced in such elongated droplets is a complicated combination of the axial flow and the outward flow along

and across the droplet, respectively. The duration of such flows that are responsible for deposition of particles will be studied.

3. Furthermore, we study the shape of the droplets during evaporation of colloidal solutions and study the effect of surfactants in the evaporation process. We will show how the small addition of surfactants can change the deposition pattern. This will be of a great interest in many scientific applications that require controlled deposition of particles on solid surfaces. We achieve this goal through creating appropriate substrate-liquid interactions, the presence of surface roughness and chemical heterogeneity. We also study the effect of substrate temperature in the deposition process and will discuss its effect on the droplet shape and the outward flow during evaporation.

These studies involve experimental and theoretical components. We will design a stage for printing the droplets and an optical setup for observing them during evaporation. We will take a numerical approach to study the evaporation of sessile droplets by developing a model that includes the physics associated with the problem.

1.4 Organization of the thesis

This thesis is organized in the following order:
Chapter 1: The sessile droplets are introduced and their significant applications in the deposition processes are discussed.
Chapter 2: The basic models of evaporation for sessile droplets are summarized, and their limitations are discussed. The evaporation-induced flow during diffusion-controlled evaporation using the basic models is studied through reviewing different models including potential flow, Stokes flow and Navier-Stokes equations. Furthermore, the deposition of particles as a result of this flow and the effect of Marangoni flow on the deposition is discussed.
Chapter 3: The experimental setup for the studies in the next chapters is discussed. The visualization methods of small droplets for each part of the study is discussed and the measurement equipment is reviewed. Furthermore, the numerical approach to model the evaporation of the spherical sessile droplets is presented followed by

the assumptions in our study.

Chapter 4: The effect of the substrate cooling on the evaporation of small droplets is discussed. We particularly show how the basic models produce a significant error in modeling the evaporation of small sessile droplets by using both experimental and numerical approaches. A dimensionless number is presented that discusses where the substrate conductivity becomes important.

Chapter 5: The evaporation of line droplets with different aspect ratio and the evaporation-induced flow inside these droplets are discussed.

Chapter 6: The effect of surface tension gradients on evaporation of colloidal suspensions is discussed. We specifically show how the shape of the droplet during evaporation can be controlled using surfactants. Furthermore, the effect of thermal Marangoni flow on the deposition is discussed.

Chapter 7: The conclusions drawn from the investigation are presented and further developments are discussed.

Chapter 2

Evaporation of sessile droplets

2.1 Introduction

The evaporation of liquid drops on a substrate is a flow problem with a free surface and plays a key role in many scientific processes. This problem has been extensively studied in the literature. Topics regarding the evaporation mechanism, the change of the droplet shape during evaporation, the evaporation-induced flow, drying and deposition patterns caused by the evaporation of colloidal suspensions have been discussed for many different applications. During evaporation, the liquid molecules transform to a vapor phase upon receiving the latent heat of evaporation and form a vapor layer at the surface of the droplet (kinetic stage). The vapor molecules at the surface diffuse into the ambient air (diffusion stage). Here we focus on the evaporation mechanism and review the main evaporation models that have been suggested for sessile droplets (Section 2.2). We then discuss the internal flow generated as a result of evaporation and will review the existing studies modeling this flow in Section 2.3. We then discuss the current models for the drying of sessile droplets of colloidal suspensions and their deposition as a result of evaporation (Section 2.3). Eventually we address the limitation of the basic models and the improvements that our model will give to the basic models (that will be discussed in the next chapter in Section 3.3).

2.2 Basic models of evaporation

The first basic model for the evaporation of sessile droplets was pioneered by Picknett and Bexon in 1977 [1], where they predicted the evaporation of drops on non-absorbing surfaces by distinguishing two separate modes of evaporation: evaporation with a constant contact angle and evaporation with a constant contact area. These evaporation modes are shown in Figure 2.1.

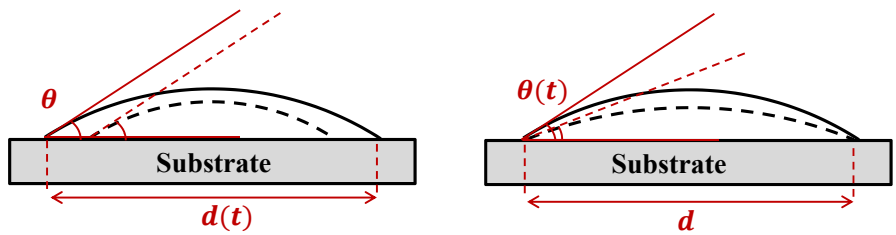

(a) Constant contact angle **(b)** Constant contact area

Figure 2.1: Evaporation modes of sessile droplets on a substrate: (a) evaporation at constant contact angle (de-pinned stage) and (b) evaporation at constant contact area (pinned stage)

In the evaporation with constant contact angle (Figure 2.1a), the contact line moves and the contact area of the droplet shrinks (de-pinned contact line). In evaporation with constant contact area (Figure 2.1b), the contact line stays fixed (pinned contact line) while the contact angle is decreasing during evaporation. They observed these evaporation modes while studying droplets of methyl acetoacetate with a mass of around 1 mg on PTFE. They investigated these two evaporation modes both theoretically and experimentally and developed a model that predicts the total evaporation rate for each mode of evaporation. They used the Maxwell analogy between the electrostatic potential and the diffusive flux of a sphere in an infinite medium and extended the model to find the evaporation flux of a sessile droplet. They calculated the capacitance of the equiconvex lens formed by the sessile droplet (shown in Figure 2.2) and used this to find the capacitance of the sessile droplet.
The lens capacitance was twice of the capacitance of the sessile droplet. They calculated the capacitance for different apex angles of the lens (i.e, θ) using Snow's

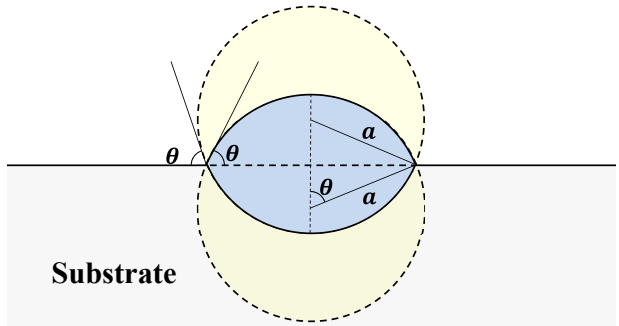

Figure 2.2: A sessil droplet with its image can be profiled as the equiconvex lens formed by two intersecting spheres with radius of a.

summation of finite series solution [17]

$$\mathscr{C}(\theta) = \begin{cases} a\left(\alpha_1\theta + \alpha_2\theta^2 - \alpha_3\theta^3\right) & \text{if } 0 \leq \theta \leq 0.175 \text{ rad} \\ a\left(\beta_0 + \beta_1\theta + \beta_2\theta^2 - \beta_3\theta^3 + \beta_4\theta^4\right) & \text{if } 0.175 \leq \theta \leq \pi \text{ rad} \end{cases}, \quad (2.1)$$

where a is the radius of the sphere and α_i and β_i are coefficient of the polynomial approximation of the series and their values are shown in Table 2.1.

Table 2.1: Coefficient of Snow's finite series in Equation 2.1 [1]

Parameter	Value
α_1	0.6366
α_2	0.09591
α_3	-0.06144
β_0	0.00008957
β_1	0.6333
β_2	0.1160
β_3	-0.08878
β_4	0.01033

Using the Maxwell analogy, Picknett and Bexon derived the evaporation rate at any contact angle of the droplet, θ, for both evaporation modes as

$$\dot{m} = 2\pi D(c_0 - c_i)\mathscr{C}(\theta), \quad (2.2)$$

where $\dot{m}$ is the evaporation mass flux, D is the molecular diffusion constant of the vapor in air, and c_0 and c_i are the vapor concentrations close to the lens surface and far from the sphere, respectively. They found this formulation for quasi-stationary Maxwellian conditions of diffusion controlled evaporation in an infinite medium. From Equation 2.2, they predicted the lifetime of a droplet with the initial mass of M_0 and initial contact angle of θ_0, and concluded that the evaporation with constant contact area (fully pinned stage) leads to a relatively shorter lifetime compared to the evaporation with constant contact angle (fully de-pinned stage). The schematic of the evaporation profiles for both evaporation modes achieved by Picknett and Bexon through theoretical formulation of Equation 2.2 is shown in Figure 2.3.

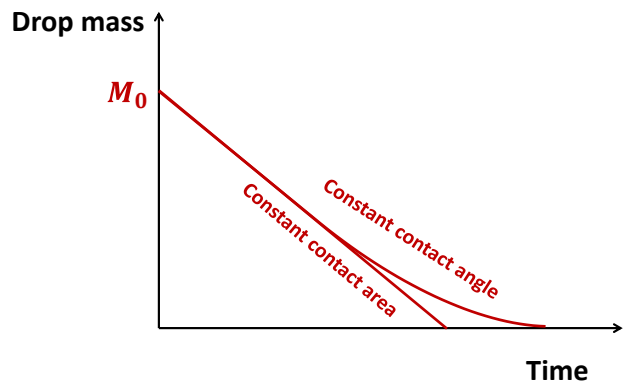

Figure 2.3: The droplet life time for both evaporation modes derived from Equation 2.2.

This was the main model used extensively in the literature to approximate the evaporation rate for the diffusion controlled evaporation. In 2001, Deegan et al. added an improvement to the model while studying the deposition of colloids from colloidal suspensions sessile droplets along the contact line [18]. They developed a model that could predict the local evaporation rate at the surface of a fully pinned sessile droplet. For the first time, they specifically reported a higher evaporation rate near the contact line of the droplet. The higher probability of escape for vapor molecules near the edge of the droplet was explained using random walk paths as shown in Figure 2.4. A molecule of vapor near the edge of the droplet, has more

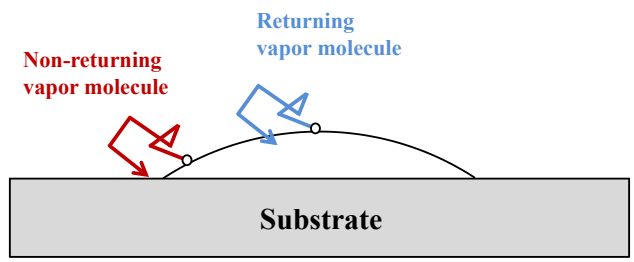

Figure 2.4: A probability of escape for vapor molecules at two different sites of the surface of the droplet for diffusion controlled evaporation. The random walk path initiated from a vapor molecule is more likely to result in a return to the surface if the starting point is further away from the edge of the droplet.

space to depart from the surface, while the random walk path suggest a higher probability of return for a vapor molecule at the center of the droplet. To model this enhanced evaporation rate toward the edge of the drop, Deegan et al. used the same analogy between a sessile droplet evaporation rate and a charged conductor electric field with the same shape (Figure 2.2). The concluded that the evaporation diverges near the contact line of the drop in the same way the electric field does near a sharp corners. Hence, the evaporation profile on the surface of the droplet close to the contact line can be presented as

$$J(r,\theta) \sim (R-r)^{-\lambda} \tag{2.3}$$

where $\lambda = (\pi - 2\theta)/(2\pi - 2\theta)$, R is the droplet radius and r is the horizontal distance from the center of the droplet as shown in Figure 2.5. Using this analogy, the evaporation rate profile over the entire surface was found as:

$$\begin{aligned} J(r,\theta) = -D(c_i - c_o)\Bigg(&\sin\left(\frac{\theta}{2}\right) \\ &+ \sqrt{2\left(x+\cos\theta\right)^3)}\int_0^\infty P_{-1/2+n\tau}(x)\,\tau\,\frac{\cosh\left(\theta\tau\right)\tanh\left(\left(\pi-\theta\right)\tau\right)}{\cosh\left(\pi\tau\right)}\mathrm{d}\tau\Bigg) \end{aligned} \tag{2.4}$$

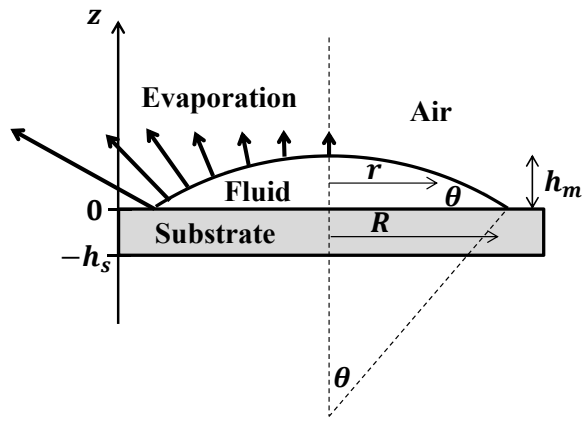

Figure 2.5: Schematic of the sessile droplet on a substrate. The evaporation rate at the surface of the droplet is enhanced toward the edge of the droplet.

where $P_{-1/2+n\tau}(x)$ is the Legendre function of the first kind and x is a parameter ranging from 0 to 1 and can be calculated from

$$r = \frac{R\sqrt{1-x^2}}{x+\cos\theta}. \tag{2.5}$$

Deegan et al. suggested a separation of variables for the evaporation rate profile at the surface of the droplet that approximates Equation 2.4 as

$$J(r,\theta) \approx J(0,\theta)\left(1-\left(\frac{r}{R}\right)^2\right)^{-\lambda}. \tag{2.6}$$

Equations 2.3 and 2.6 show that for diffusion controlled evaporation, the evaporation increases toward the corners when $r \to R$.

Hu and Larson [19] continued this study and investigated the enhanced evaporation rate near the corner by solving the boundary value problem numerically and compared their results with experiments. The mathematical model for the diffusion controlled evaporation that they developed was based on solving for the quasi-steady state diffusion of the saturated vapor at the surface of the droplet into the

ambient air. Modeling the diffusion of the vapor molecules then yields

$$\nabla^2 C = \frac{\partial C}{\partial t}, \tag{2.7}$$

where C is the vapor concentration around the droplet and t is time. In the case of water droplets, the evaporation process is slow and the time that it takes for the vapor to adjust the concentration at the surface is fast compared to the diffusion time scale. Hence the evaporation can be considered to be quasi-steady and the time derivative vanishes. The diffusion model then changes to the Laplace equation

$$\nabla^2 C = 0. \tag{2.8}$$

A non-homogeneous Dirichlet boundary condition (i.e. $c_i \neq c_0$) drives the vapor from the free surface of the droplet to the ambient air and evaporation occurs. For a spherical water droplet with the parameters shown in Figure 2.5, the boundary conditions in 2D can be written as:

1. At the surface of the droplet, the concentration of the vapor is equal to the saturated vapor concentration:

$$C|_{interface} = c_i = C_v|_{T_{interface}}. \tag{2.9}$$

2. Far from the surface of the droplet, we have

$$C|_{ambient} = c_o = \phi \; C_v|_{T_{ambient}}, \tag{2.10}$$

   where ϕ is the relative humidity of water in air.

3. No diffusion through the substrate:

$$\nabla C = 0. \tag{2.11}$$

Similar boundary conditions can be written for line droplets in 3D (Equations 5.22 to 5.24) in Chapter 5.

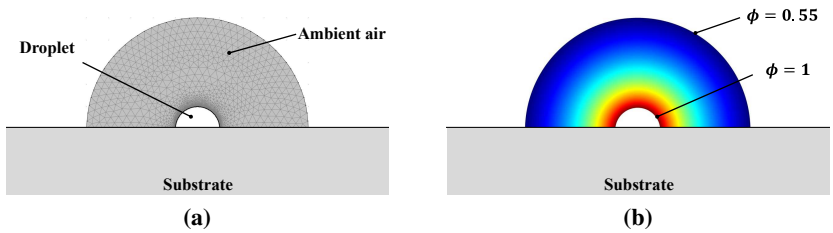

Figure 2.6: The domain mesh (a) and the solution of the Laplace equation for diffusion of the water vapor molecule with the concentration of $C_v = 1.9 \times 10^{-8}\,\mathrm{g/mm^3}$ at the surface of the droplet into the ambient air with the relative humidity of 55%, i.e. $\phi = 0.55$ (b).

The evaporation flux

$$\vec{J}(x,y,z) = D\vec{\nabla}C \tag{2.12}$$

can be calculated from the vapor concentration solutions of the Laplace equation with the boundary conditions above (Equations 2.9 to 2.11) using Finite Element Method (FEM) with the mesh structure shown in Figure 2.6a are shown in Figure 2.6b. The evaporation flux using Equation 2.12 is shown in Figure 2.7 for two different contact angles of $\theta = 90^\circ$ and $\theta = 60^\circ$. As shown in Figure 2.7, the evaporation profile is uniform over the surface when the contact angle is equal to 90° (hemisphere). When the contact angle is reduced below 90° as shown for a droplet with the contact angle of 60°, the evaporation is enhanced toward the corners until it becomes singular at the contact line. This is consistent with the previous results by Deegan et al. [18].

Hu and Larson solved Equation 2.8, with the boundary conditions (Equations 2.9 to 2.11) numerically and suggested a formula for the total evaporation mass flux:

$$\frac{\mathrm{d}M}{\mathrm{d}t} = -\pi RD(1-\phi)C_v\left(0.27\theta^2 + 1.30\right). \tag{2.13}$$

Popov [20] solved the Laplace equation explicitly and found the evaporation mass flux as

$$\frac{\mathrm{d}M}{\mathrm{d}t} = -\pi RD(1-\phi)C_v f(\theta), \tag{2.14}$$

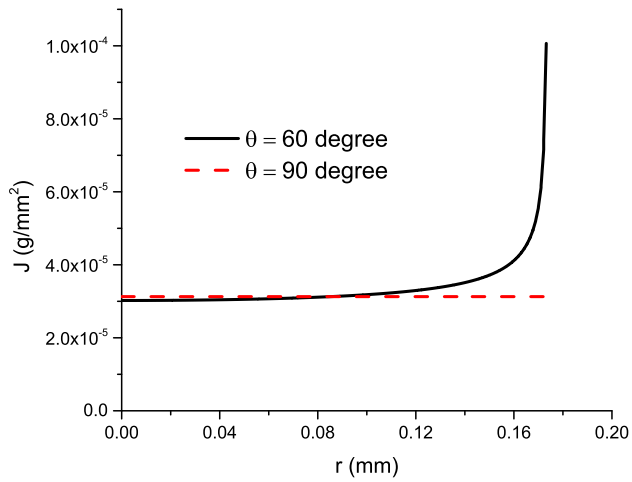

Figure 2.7: The evaporation flux, J for a water droplet with the radius of $R = 0.17$ mm into the ambient air with the relative humidity of 55% at room temperature for different contact angles of $\theta = 90^\circ$ and $\theta = 60^\circ$.

where

$$f(\theta) = \frac{\sin\theta}{1+\cos\theta} + 4\int_0^\infty \frac{1+\cosh(2\theta\tau)}{\sinh(2\pi\tau)} \tanh\left[(\pi-\theta)\,\tau\right] \mathrm{d}\tau. \tag{2.15}$$

By writing the droplet volume in terms of θ (from Equation A.13) and inserting it into Equation 2.14, the rate of change of the contact angle for a fully pinned droplet (i.e. R remains constant during evaporation) was found as

$$\frac{\mathrm{d}\theta}{\mathrm{d}t} = -\frac{D(1-\phi)C_v}{\rho R^2}(1+\cos\theta)^2 f(\theta), \tag{2.16}$$

where ρ is the density of the fluid. Also, by rewriting Equation 2.16 as

$$\frac{\mathrm{d}\theta}{(1+\cos\theta)^2 f(\theta)} = -\frac{D(1-\phi)C_v}{\rho R^2}\mathrm{d}t, \tag{2.17}$$

the total evaporation time can be calculated as

$$T_f = \frac{\rho R^2}{D(1-\phi)C_v} \int_0^{\theta_c} \frac{\mathrm{d}\theta}{(1+\cos\theta)^2 f(\theta)}, \tag{2.18}$$

where θ_c is initial equilibrium contact angle of the droplet. By defining

$$\hat{t} = \frac{(1-\phi)C_v}{\rho} \frac{t}{R^2/D} \tag{2.19}$$

and

$$\hat{M} = \frac{M}{\rho R^3}, \tag{2.20}$$

Equations 2.14 and 2.16 are simplified to

$$\frac{\mathrm{d}\hat{M}}{\mathrm{d}\hat{t}} = -\pi f(\theta) \tag{2.21}$$

and

$$\frac{\mathrm{d}\hat{\theta}}{\mathrm{d}\hat{t}} = -(1+\cos\theta)^2 f(\theta), \tag{2.22}$$

and become independent of the environmental conditions of the evaporation. The simplified rate of change in the contact angle and the evaporation mass flux (defined in Equations 2.19 and 2.20) is shown in Figure 2.8a. Also, the change of the contact angle versus simplified time (defined in Equation 2.22) was found by solving the ordinary differential equation numerically (Equation 2.17) and is shown in Figure 2.8b. Popov estimated $-\mathrm{d}\hat{M}/\mathrm{d}\hat{t} = \pi f(\theta) \cong 4$ for small contact angles (as can be seen from Figure 2.8a) and was able to calculate the evaporation mass flux from Equation 2.14 as

$$\frac{\mathrm{d}M}{\mathrm{d}t} = -4RD(1-\phi)C_v, \tag{2.23}$$

and the rate of the contact angle change from Equation 2.16 as

$$\frac{\mathrm{d}\theta}{\mathrm{d}t} = -\frac{16D(1-\phi)C_v}{\rho\pi R^2}. \tag{2.24}$$

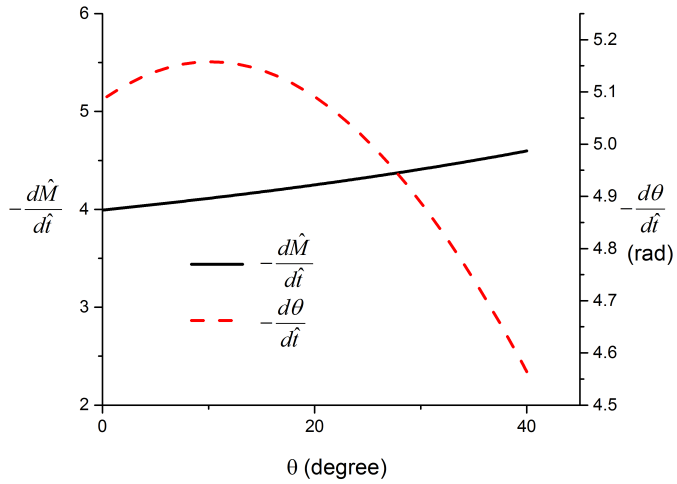

(a)

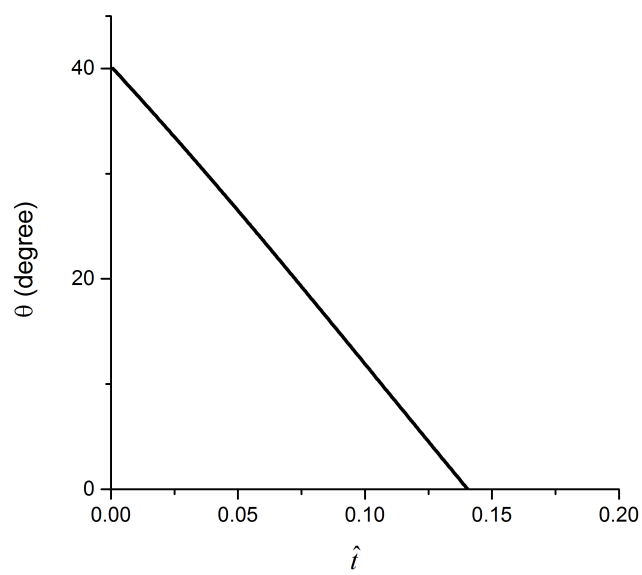

(b)

Figure 2.8: (a) The rate of change of the contact angle and the evaporation mass flux during the evaporation at constant contact area (fully pinned stage) with the initial contact angle of $\theta_c = 40$; (b) contact angle during evaporation versus $\hat{t}$.

This yields the total evaporation time

$$T_f = \frac{\pi \rho R^2 \theta}{16 D (1-\phi) C_v} \tag{2.25}$$

and the droplet mass

$$M = \frac{\pi \rho R^3 \theta}{4} \left(1 - \frac{t}{T_f}\right) \tag{2.26}$$

as a function of time. Equation 2.26 shows the linear time dependence of mass during most of the evaporation process. The basic evaporation models, showed good agreement with the experiments at various evaporation conditions [1, 19–22]. Hu and Larson specifically showed that their evaporation model predicts the experimental results with an error around 10 % for droplets with 0.5 mm $< R <$ 1 mm in radius. They also observed that the experimental results deviate significantly from the basic evaporation models by up to 25% for small droplets with $R <$ 0.5 mm.

2.3 Evaporation-induced flow

During the evaporation of sessile droplets with a pinned contact line, the evaporation rate increases toward the corner of the droplets. The amount of fluid removed by the evaporation needs to be replenished to keep the substrate wet and to keep the contact line pinned. Therefore, a flow is generated from the center toward the contact line. This viscous flow for sessile droplets with a pinned contact line, that is also referred to in the literature as the "evaporation-induced flow", has always an outward direction. For colloidal suspensions, this internal flow carries the suspension particles with the fluid toward the contact line where they deposit in a ring shape [18]. This is often referred to as the "coffee-stain" effect (Figure 2.9a).
Deegan et al. [18] quantified the evaporation-induced flow for the first time using the evaporation model in Equation 2.6. The average velocity of a column shown in Figure 2.10 was found from the evaporation rate through mass conservation

$$\rho \frac{\partial h_r}{\partial t} = -\rho \frac{1}{r} \frac{\partial (r h_r v_r)}{\partial r} - J(r,t) \sqrt{1 + \left(\frac{\partial h_r}{\partial r}\right)^2}, \tag{2.27}$$

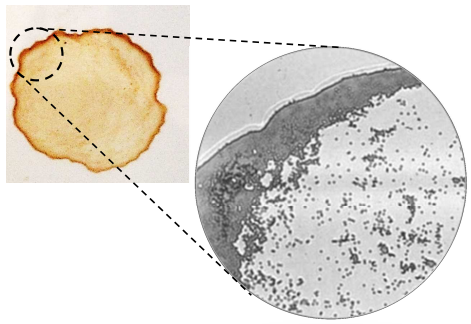

(a)

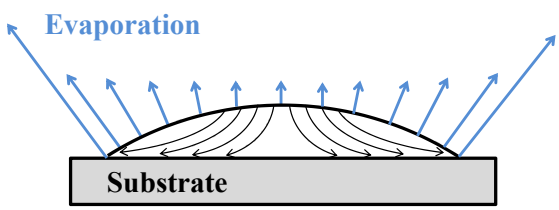

(b)

Figure 2.9: An internal flow is generated inside the sessile droplet as a result of evaporation that carries the fluid toward the corners: (a) top view of a ring deposition after drying a coffee droplet, (b) outward evaporation-induced flow inside a sessile droplet

where h_m and h_m are the column heights at the center and at the distance r from the center, respectively. With $J(0,\theta)$ from Equation 2.4, and with h_r versus R, r and θ from Equation A.17, the average velocity of the column v_r in 2.27 was calculated. Tarasevich [23] suggested the potential flow assumption to solve the evaporation-induced velocity field for a hemispherical droplet and showed, to the best of our knowledge for the first time, the qualitative picture of the flow. The potential flow was solved for the hemisphere (with constant evaporation flux J_0) as

$$J(r,\theta) = J(0,\pi/2) = J_0 = -\frac{\pi D(1-\phi)c_v}{R}. \tag{2.28}$$

The potential flow field equation

$$\nabla^2\varphi = 0, \tag{2.29}$$

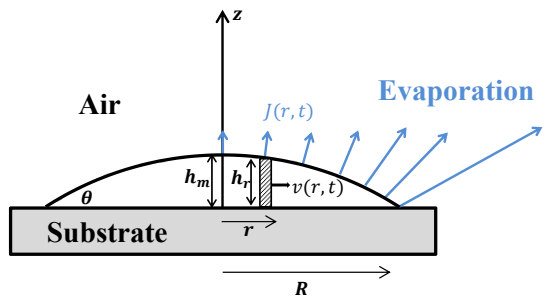

Figure 2.10: The average evaporation-induced flow in a vertical fluid column at a distance r from the center. The flux leaving the top surface is equal the to local evaporation rate at the surface $J(r,t)$.

where φ is the velocity potential then was solved analytically with the following boundary conditions:

1. Geometrical symmetry at $r = 0$ gives

$$\frac{\partial \varphi}{\partial r} = 0. \tag{2.30}$$

2. No-flow through the substrate condition at $z = 0$ gives:

$$\frac{\partial \varphi}{\partial z} = 0. \tag{2.31}$$

3. The kinematic boundary condition at the surface of the droplet is achieved by writing the conservation of mass

$$\vec{v}_n = \vec{U}_n - \frac{\vec{J}}{\rho}, \tag{2.32}$$

where $\vec{v}_n$ is the velocity of the fluid and $\vec{U}_n$ is the normal velocity of the surface as shown for a liquid element at the surface in Figure 2.11.

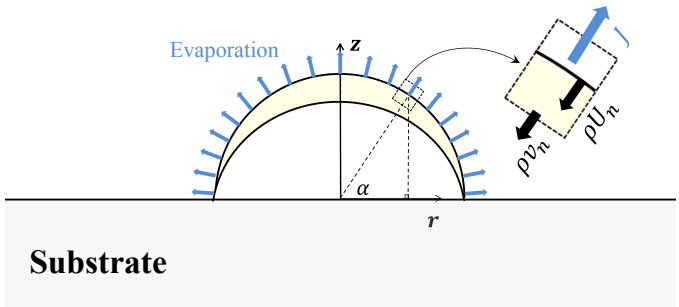

Figure 2.11: The air-liquid interfaces moves as a result of the evaporation. Using the conservation of mass for an infinitesimal element at the surface, the velocity of the fluid normal to the boundary, $\vec{v}_n$ was found by subtracting the evaporation flux, $\vec{J}/\rho$ from the interface velocity $\vec{U}_n$.

Tarasevich approximated the velocity of the interface during evaporation for a hemispherical droplet as

$$\left|\vec{U}_n\right| = U_0 \cos\alpha, \tag{2.33}$$

where

$$U_0 = \frac{\partial h_m}{\partial t}. \tag{2.34}$$

is the velocity of the interface at the center and α is an angle shown in Figure 2.11. Using the simplified assumption of a constant flux over the surface of the hemisphere, we can write

$$\int J \mathrm{d}s = J_0(2\pi R^2) = \rho \frac{\mathrm{d}V}{\mathrm{d}t}, \tag{2.35}$$

where $\mathrm{d}V/\mathrm{d}t$ can be approximated as $\pi R^2 U_0$. Hence,

$$U_0 = \frac{2J_0}{\rho}. \tag{2.36}$$

By inserting U_0 into Equation 2.33 and then Equation 2.32, we will find the normal component of the fluid velocity at the interface of a hemisphere as:

$$\vec{v}_n = -\frac{J_0}{\rho}\left(1 - 2\cos\alpha\right) \tag{2.37}$$

or

$$\vec{v}_n = -\frac{J_0}{\rho}\left(1 - \frac{2r}{\sqrt{r^2 + h_r^2}}\right). \tag{2.38}$$

Petsi and Burganos [24] extended this work and calculated the evaporation-induced flow by solving the velocity potential formulation for a half-cylinder on a substrate. They assumed Equation 2.29 with the boundary conditions in Equations 2.30 to 2.32 for both fully pinned and fully de-pinned droplets. By assuming a constant evaporation flux at the surface ($J(0, \pi/2) = J_0$), they solved the potential field analytically for the fully pinned droplet and suggested the potential field as

$$\varphi(r, \alpha) = \frac{J_0 R}{\rho} \sum_{m=1}^{\infty} \frac{(r/R)^{2m} \cos(2m\alpha)}{m\left(4m^2 - 1\right)}. \tag{2.39}$$

The velocity field and streamlines produced by the potential flow of Equation 2.39 are shown in Figure 2.12. They approximated the potential field of Equation 2.39 with a closed-form expression

$$\varphi(r, \alpha) \approx \frac{J_0}{\rho}\left(\frac{r^2\cos(2\alpha)}{3R^2} + \frac{r^4\cos(4\alpha)}{30R^4}\right) \tag{2.40}$$

with 99% accuracy except for the area close to the air-fluid interface.
They solved the potential flow for the fully de-pinned half-cylinder droplet of infinite length (assuming that the contact angle, $\theta = \pi/2$ remains constant during evaporation) with the constant evaporation flux at the surface of the droplet J_0. The boundary conditions in Equations 2.30 and 2.31 will be the same for fully de-pinned droplets. However, the mass balance at the air-fluid interface of droplets with a moving contact line at constant evaporation flux yields a constant interface velocity

$$\left|\vec{U}_n\right| = \frac{\mathrm{d}R}{\mathrm{d}t} = -\frac{J_0}{\rho}. \tag{2.41}$$

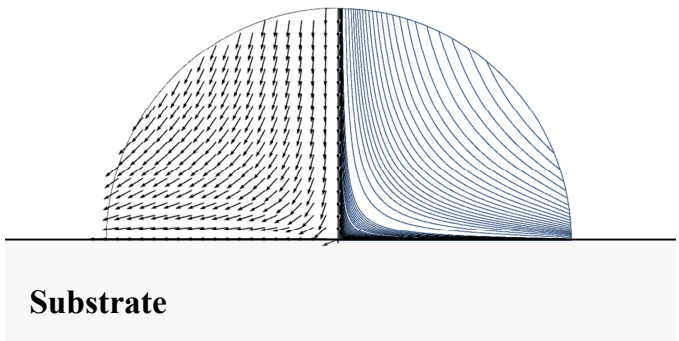

Figure 2.12: The velocity field (left) and streamlines (right) of potential flow inside a half-cylinder as a result of evaporation.

Later on, they extended this work by solving the potential flow for any contact angle for both fully pinned and fully de-pinned evaporation modes [25]. To do this, $\vec{U}_n$ in Equation 2.33 was calculated for any contact angle as

$$\left|\vec{U}_n\right| = J_{TOT} \frac{\sin\theta \left(\cos\theta - \kappa\sqrt{1-(r/R)^2\sin^2\theta}\right)}{2R\left(\sin\theta - \theta\cos\theta\right)}, \tag{2.42}$$

where J_{TOT} is the total evaporation rate per unit length of the cylinder and κ is defined as

$$\kappa = \begin{cases} 1 & \text{if } 0 \leq \theta \leq \pi/2 \\ -1 & \text{if } \pi/2 \leq \theta \leq \pi \end{cases}. \tag{2.43}$$

Masoud and Felske [26] solved the velocity field using Stokes flow when inertial forces are negligible for both spherical and cylindrical droplets with the initial radius less than 1 mm where the Reynolds number is around 10^{-3}. They solved the Stokes flow field for both fully pinned and fully de-pinned sessile droplets at any contact angle considering the non-uniform evaporation flux over the surface. The velocity stream function then yields the biharmonic equation

$$\nabla^4\psi = 0. \tag{2.44}$$

Their results showed good qualitative agreement with the velocity field described by potential flow. They specifically showed that while the vertical velocity components (v_z) are similar for both solutions, the radial velocity components (v_r) of the solutions give rather different velocity profiles (as shown in Figure 2.13). The main reason behind this difference is the no slip boundary condition that is valid for Stokes flow field (for a viscous fluid) that results in a zero velocity at the substrate surface.

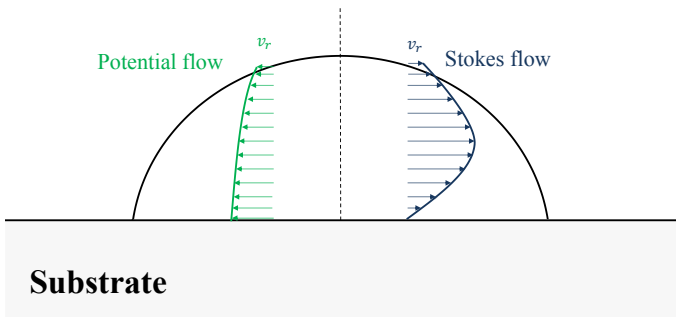

Figure 2.13: The radial velocity component from potential flow (left) and Stokes flow (right).

Hu and Larson [27] solved the full Navier-Stokes equation for small droplets with diffusion controlled evaporation. Assuming an incompressible quasi-steady flow with negligible convective acceleration for a spherical droplet shown in Figure 2.5, yields the continuity equation

$$\frac{1}{r}\frac{\partial v_r}{\partial r} + \frac{\partial z}{\partial z} = 0 \tag{2.45}$$

and the momentum equations in r and z direction

$$\begin{aligned} \frac{1}{\mu}\frac{\partial P}{\partial r} &= \frac{\partial}{\partial r}\left(\frac{1}{r}\frac{\partial (r v_r)}{\partial r}\right) + \frac{\partial^2 v_r}{\partial z^2}, \\ \frac{1}{\mu}\frac{\partial P}{\partial z} &= \frac{\partial}{\partial r}\left(r\frac{\partial v_z}{r}\right) + \frac{\partial^2 v_z}{\partial z^2}, \end{aligned} \tag{2.46}$$

where P is the pressure and μ is the viscosity of the fluid. They solved the Navier-Stokes equation with the following boundary conditions and assumptions:

1. For thin droplets the lubrication theory assumption can be used to estimate the vertical velocity profile as

$$v_z = \xi_1 z^2 + \xi_2 z + \xi_3, \tag{2.47}$$

where ξ_i are the coefficient that need to be determined using the boundary conditions.

2. The zero shear-stress boundary condition at the air-fluid interface yields

$$\left.\frac{\partial v_r}{\partial z}\right|_{z=h_r} = -\left.\frac{\partial v_z}{\partial r}\right|_{z=h_r}. \tag{2.48}$$

3. The kinetic boundary condition at the surface is

$$v_z|_{z=h_r} = \frac{\partial h_r}{\partial t} + \frac{J(r,t)}{\rho}. \tag{2.49}$$

Hu and Larson used an approximation for the rate of height change over time as

$$\frac{\partial h_r}{\partial t} = \frac{\partial h_m}{\partial t}\left(1-(r/R)^2\right) = 2\frac{\mathrm{d}M}{\mathrm{d}t}\frac{1-(r/R)^2}{\rho\pi R^2}. \tag{2.50}$$

4. The no-slip boundary condition at the substrate surface for the fully pinned evaporation mode gives

$$v(r,z)|_{z=0} = 0, \tag{2.51}$$

and $\xi_3 = 0$ in Equation 2.47.

5. For a flat droplet, they assumed that

$$\frac{\partial v_z}{\partial r} \approx \frac{\partial}{\partial r}\left(v_z|_{z=h_r}\right). \tag{2.52}$$

(6) By assuming a linear rate of decrease of the droplet height during evaporation, then the rate of height change at the center was written as

$$\frac{\partial h_m}{\partial t} \approx -\frac{H}{T_f}, \tag{2.53}$$

where H is the initial height of the droplet, i.e. $H = h_m|_{t=0}$.

With these boundary conditions and assumptions, Hu and Larson derived an expression for the dimensionless vertical and radial velocities

$$\begin{aligned} \hat{v}_r &= \frac{3}{8}\frac{1}{1-\hat{t}}\frac{1}{\hat{r}}\left((1-\hat{r}^2)-(1-\hat{r}^2)^{-\lambda}\right)\left((\hat{z}/\hat{h})^2-2(\hat{z}/\hat{h})\right) \\ &+ \frac{\hat{r}H^2\hat{h}}{R^2}\left(\hat{J}\lambda(1-\hat{r}^2)^{-\lambda-1}+1\right)\left((\hat{z}/\hat{h})-3/2(\hat{z}/\hat{h})^2\right) \end{aligned} \tag{2.54}$$

and

$$\begin{aligned} \hat{v}_z &= \frac{3}{4}\frac{1}{1-\hat{t}}\left(1+\lambda(1-\hat{r}^2)^{-\lambda-1}\right)\left(1/3(\hat{z}^3/\hat{h}^2)-(\hat{z}^2/\hat{h})\right) \\ &+ \frac{3}{2}\frac{1}{1-\hat{t}}\left((1-\hat{r}^2)-(1-\hat{r}^2)^{-\lambda}\right)\left(1/2(\hat{z}^2/\hat{h}^2)-1/3\hat{z}^3/\hat{h}^3\right)\hat{h}_m \\ &- \frac{H^2}{R^2}\left(\hat{J}\lambda(1-\hat{r}^2)^{-\lambda-1}+1\right)(\hat{z}^2-(\hat{z}^3/\hat{h})) \\ &+ \frac{\hat{r}H^2}{R^2}\hat{J}\lambda(\lambda+1)\left(1-\hat{r}^2\right)-\lambda-2\left(\hat{z}^2-(\hat{z}^3/\hat{h})\right) \\ &- \frac{\hat{r}H^2}{R^2}\left(\hat{J}\lambda\left(1-\hat{r}^2\right)^{-\lambda-1}+1\right)\left(\hat{z}^3/\hat{h}^2\right)\hat{h}_m, \end{aligned} \tag{2.55}$$

where $\hat{v}_r = v_r T_f/R$, $\hat{v}_z = v_z T_f/H$, $\hat{r} = r/R$, $\hat{z} = z/H$, $\hat{h} = h_r/H$, $\hat{h}_m = h_m/H$ and λ and T_f were previously defined in Equations 2.6 and 2.25, respectively.

2.4 Drying of colloidal suspension droplets

During the evaporation of sessile droplets from colloidal suspensions, the internal flow carries particles and they precipitate until the droplet fully dries. The deposition of the particles from the colloidal suspensions as a result of evaporation has been extensively studied in various geometries for different suspensions and solvents. However the first mathematical model for deposition of colloids as a result

of evaporation-induced flow was suggested by Deegan et al. [18]. They showed that how evaporation generates an outwards flow inside the droplet which can cause particles to form a ring deposition near the contact line as the droplet dries. They calculated this flow for a vertical liquid column within the droplet shown in Figure 2.10. They assumed a uniform concentration in the vertical column during the evaporation of a sessile droplet in still air with fully pinned contact line. Therefore, the mass conservation equation for particles gives

$$\frac{\partial}{\partial t}(c_r h_r) + \frac{1}{r}\frac{\partial}{\partial r}(r c_r h_r v_r) = 0, \tag{2.56}$$

where c_r is the concentration of the particles in the vertical column. The mass of the deposition ring then was found by subtracting the mass of the particles in the droplet at a later time from the mass of particles at $t = 0$. For thin droplets, they suggested the mass of the deposition ring to change in time as

$$m_R = m_0 \left(1 - (1 - t/T_f)^{(1+\lambda)/2}\right)^{2/(1+\lambda)} \tag{2.57}$$

where m_R and m_0 are the deposition ring and the total mass of the particles at $t = 0$. Knowing the mass of the ring at any time, they suggested a formula for the width of the deposition band based on experiments as a function of time as

$$\delta(t) = \frac{m_R}{t^{2/(1+\lambda)}} \frac{2}{\chi \tan\theta} \left(\frac{2^{\lambda} \pi R^{2-\lambda} \tan\theta}{(\mathrm{d}V/\mathrm{d}t)(1+\lambda)} \right)^{2/(1+\lambda)}, \tag{2.58}$$

where χ is the number of particles per until volume at $t = 0$.
Popov [20] continued this and using the basic model of evaporation, and suggested a model to calculate the width of the deposition ring. In this model, a growing deposit phase of particles was defined that is formed by a viscous particle flow as a result of evaporation (Figure 2.14). By writing the global and local mass conservation of particles and liquid, they were able to estimate the width of the deposition band as

$$\delta(t) = \sqrt{\frac{\chi}{c_0}} R \frac{(3\hat{t})^{2/3}}{2^{7/3}}. \tag{2.59}$$

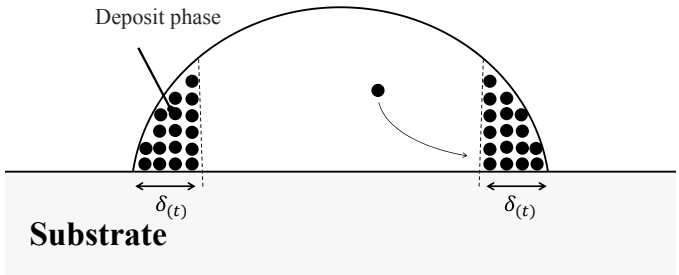

Figure 2.14: Evaporation-induced flow carries particles toward the corners and forms a deposit phase near the contact line of a sessile droplet.

Bhardwaj et al. [28] and Petsi and Burganos [29] investigated the pattern formation of microsphere in colloidal suspensions using Lagrangian and Brownian dynamics. Park and Moon [30] demonstrated a controlled ring deposition of a uniform particle layer within picoliter sessile droplets. They showed that surfactant mixed-solvents will result in vanishing ring deposition. They also found a critical concentration of particles above which the ring deposition is reduced [30]. This is in contrast to Popov's model that predicts a wider ring deposition at higher particle concentrations. The main reason of the ring deposition suppression at higher concentrations was the Marangoni flow that produced a backward flow that countered the outward evaporation-induced flow [30]. This Marangoni flow was produced because of the surface tension gradients that can be generated conceivably as a result of particle concentration or a thermal gradient inside the droplet.

Hu and Larson [27] studied the thermal Marangoni flow during quasi-steady state evaporation of a sessile droplets by assuming the convective heat transfer to be negligible and solved the conductive heat transfer across the droplet using the Laplace equation for temperature. They showed that the latent heat of evaporation induces an inward thermal Marangoni flow near the fluid-air interface that carries the particles toward the center. The velocity profile under the presence of the Marangoni effect is shown in Figure 2.15. At the surface of the droplet, the Marangoni flow is zero at the center (due to axisymmetry) and is enhanced toward the contact line. This inward flow acts against the outward evaporation-induced flow at the surface until canceling it out at the stagnation point beyond which the direction of the sur-

face flow reverses (Figure 2.15). They confirmed the effect experimentally later by showing that the inward Marangoni flow reduces the ring deposition [31].

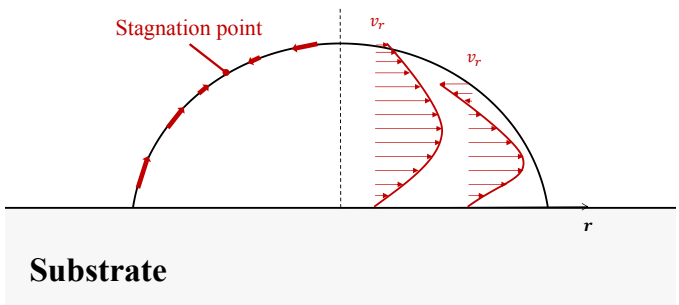

Figure 2.15: Marangoni flow produces an inward flow that counters the outward evaporation-induced flow for sessile droplets during the pinned stage.

2.5 Conclusion

The basic models of evaporation for a sessile droplet on a substrate assume isothermal diffusion of vapor into the ambient air. By assuming isothermal diffusion, i.e. $c_v|_{\text{interface}} \approx c_v|_{\text{ambient air}}$, the temperature only affects the problem by changing c_v and D. Using this assumption, the Laplace equation was solved for the diffusion-controlled evaporation at a quasi-steady state. The total evaporation time was then calculated by finding the amount of fluid removed by evaporation in a small time step and then by integrating these until the entire evaporation of the droplet. The basic models showed an enhanced evaporation rate near the contact lines for droplets with $\theta < 90°$. However, while these models predict fairly well the evaporation of droplets with 0.5 mm $< R <$ 1 mm, they produce significant errors for smaller droplets. While to date, the main reason behind this significant error for small droplets is not known, Hu and Larson [19] rejected the effect of the substrate and the droplet thermal conductivities as the maximum temperature change across the droplet during evaporation is less than 0.02 °C for droplets with $R <$ 1 mm, which has negligible effect on c_v and D. In Chapter 4, we study the effect of temperature and the important effect of substrate conductivity on evaporation of small droplets and we will discuss that while this temperature change has

negligible effect on c_v and D, it defines the rate limiting step of heat transfer to the surface to provide the latent heat of evaporation.

The enhanced evaporation near the contact line induces a flow inside the droplet. The basic theories that model this flow were discussed. The evaporation-induced flow solutions for a spherical droplet and an infinite cylinder (liquid line), for both evaporation modes (i.e. fully pinned and fully de-pinned) were shown. The comparison of the Navier-Stokes, Stokes flow, Lubrication theory and potential flow shows that a qualitative agreement between the results exists. The no-slip boundary condition for viscous flow causes the main difference between the results of the inviscid and viscous flows.

Finally, the deposition of particles of colloidal suspensions during evaporation as a result of internal flows shows that a ring deposition forms during the evaporation of fully-pinned droplets. The main studies that model the deposition ring as a result of the evaporation-induced flow was shown, and the suppression of the ring band as a result of Marangoni flow was discussed.

Chapter 3

Experimental and numerical approach

3.1 Introduction

The study of small sessile droplets in the order of 50 μm $< R <$ 1 mm needs careful deposition and measurement techniques. The small size of the droplets increases their sensitivity to environmental condition that could produce a significant error in the measurement and interpretation of the data. In this chapter, the methods that were used in our experiments to print the droplets at the micro scale, to control the ambient conditions, to visualize the droplet during evaporation and to measure the deposition pattern after evaporation will be explained (Section 3.2).

As mentioned in the previous chapter, the current evaporation methods produce a significant error for small droplets with $R <$ 500 μm. In this chapter, the numerical approach that we used to overcome these limitations will be presented and discussed (Section 3.3).

3.2 Experimental setup

3.2.1 Printing stage

To print spherical and cylindrical droplets, a portable micro patterning stage was designed. The system consist of: 1) a motorized linear stage for printing the line droplets, 2) a micro nozzle for printing droplets by dispensing liquid from a container onto the substrate, 3) a micro positioner to adjust the distance of the nozzle from the substrate, 4) a pressure manifold that controls the pressure of the liquid inside the micro nozzle. The printing stage setup is shown in Figure 3.1. The

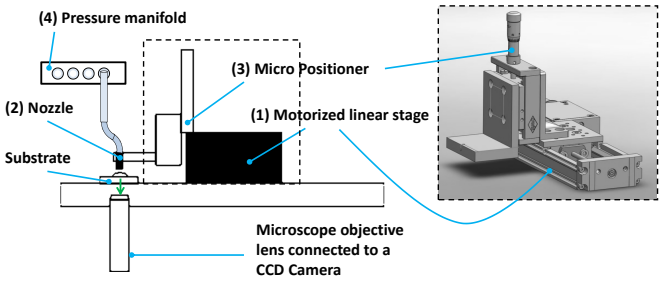

Figure 3.1: The portable micro printing setup. A motorized linear stage from Zaber Technologies Inc. was used to control the place and speed of the micro nozzle.

motorized linear stage is the model T-LSM050A-KT03 from Zaber Technologies Inc. (Vancouver, BC V6P6P2, Canada) with a 50 mm range of travel. MicroFab (Plano, TX 75074 USA) MJ-ABP-01 dispensing nozzles with a diameter of 80 mm were used for printing droplets. The model 2210-CE amplifier from Trek Inc. (NY 14103, United States) is used to increase the power of the signal to the micro nozzle. A computer code was written in C$^\sharp$ to synchronize the printing sequence with the motion of the stage so that the desired length and width of the line droplets or an array of point droplets can be printed. The micro positioner is the model MT 45-13-X-MS measuring stage from the OWIS GmbH (Im Gaisgraben 7, 79219 Staufen, Germany), with central micrometer with a measuring range of 12 mm.

The PID pressure controller is the system MFCS-8C 1000 from Fluigent(94800 Villejuif, France).

3.2.2 Droplet visualization and measurements

To understand the behavior of small droplets, precise visualization methods and careful measurements of parameters are required. Here we show the tools that are used to capture the droplet shape (the contact line and the contact angle) during evaporation while measuring and controlling the environmental conditions such as humidity and temperature.

Contact angle measurement

As described earlier, one of the key points in understanding the evaporation of sessile droplets and determining the deposition sites of colloidal suspensions is the behavior of the contact line, i.e. whether it is pinned or de-pinned. In our experiments we are using colloidal suspensions of nano particles at different particles concentrations. In evaporation of colloidal suspensions, depending on the initial concentration of the solutes, we observed a combination of both pinned and de-pinned for the contact line. A series of experimental measurements is conducted to find the receding contact angle θ_r for different substrates and for different types of particles at different sizes. The experimental data collected in this section will be used as the material properties and coefficients for the numerical approach in Section 3.3. To investigate these parameters, we use a Theta Lite optical tensiometer from Attension/Biolin Scientific (SE-107 24 Stockholm, Sweden) to measure the contact angle and radius of the droplet during the evaporation. Images are taken at 1 Hz with the resolution of 640×480 pixels using a Firewire digital video camera with the speed of 60 fps (frames per second) . Images are processed using the OneAttension software and the Young-Laplace fitting method is used to find the droplet profile. The portable printing stage (Figure 3.1) is used to dispense controlled volumes of the liquid onto the substrate to generate droplets at different initial radii.

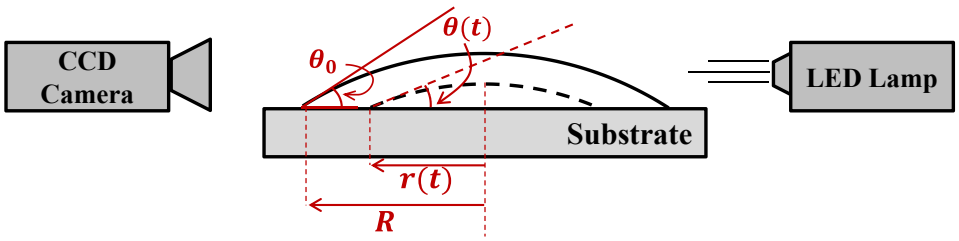

Figure 3.2: The experimental setup for investigating the contact line and contact angle during the evaporation. The experiment was illuminated using LED based background lighting.

Velocity measurement

To measure the evaporation-induced velocity field of sessile droplets, several techniques have been used by different researchers. For spherical droplets, a cross sectional view across the center gives a sufficient understanding of the velocity profile due to the axisymmetric shape of the droplet [11]. Kang et al. suggested a quantitative visualization technique to correct the effect of light refraction near the surface of the droplet [32]. However, to capture the flow inside droplets with a small diameter ($R < 500$ µm) a rather large lens with high magnification is required to observe the flow. We use an inverted microscope image (with the objective lens magnification of 40×) to capture the horizontal flow near the substrate while observing the contact line movement in real time. FS04F fluorescent microspheres beads from Bangs Laboratories, Inc. (IN 46038, United States) are used for flow visualization. The images of microspheres are captured at two different frame rates of 50 fps (using a Imager sCMOS Camera - with the resolution of 5.5 Mpixels) and 2000 fps (using a Phantom M4 high-speed camera). The horizontal velocity field was then calculated using micro particle image velocimetry (PIV) through Davis 8.0 software from Lavision (MI 48197, United States) as shown in Figure 3.3.

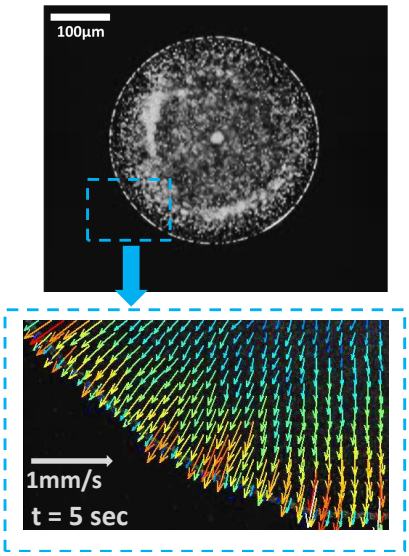

Figure 3.3: The horizontal velocity near the substrate was observed using an inverted microscope stage and the velocity was measured using PIV.

Temperature and humidity measurement

As mentioned in Chapter 2, ambient temperature and humidity play an important role in evaporation rate. Also, in Chapter 3 and Chapter 6.1, we will discuss the important influence of the substrate temperature on the evaporation of sessile droplets and the deposition at the contact line in colloidal suspensions. The humidity and temperature was measured using a SHTC1 humidity sensor and a STS21 temperature sensor from Sensirion (8712 Staefa ZH, Switzerland).

To control the temperature of the substrate a closed loop temperature control system is designed as shown in Figure 3.4. A CZ1-1.0-127-1.27 Peltier device from Tellurex (MI 49686, United States) is attached from the cold side to the substrate to control the temperature while the excessive heat is dissipated from the hot side. We use a temperature sensor mounted on the Peltier element, a power supply, and a data acquisition unit (DAQ) and CPU to communicate between each. Using this self-regulating setup, a temperature range of 15 °C to 40 °C with an accuracy of ± 0.1°C for the substrate was achieved. The temperature of the surface of the

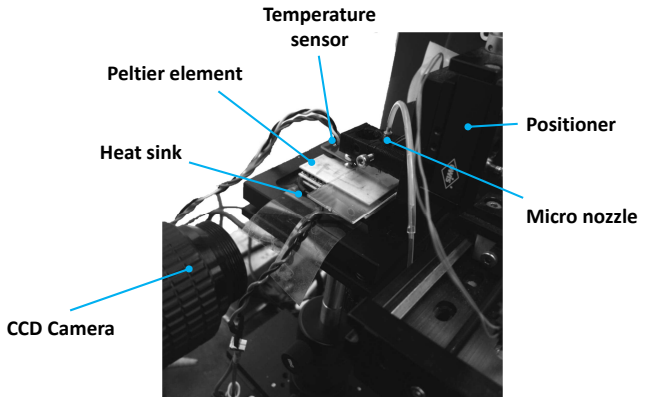

Figure 3.4: The temperature of the substrate is controlled using a Peltier device in a closed loop temperature control circuit. The signal from the temperature sensor attached to the substrate is used to provide the feedback signal to the controller.

droplet during evaporation is measured using IR-TCM-384 infrared thermographic camera from Jenoptik (07743 Jena, Germany) as shown in Figure 3.5.

Deposition measurement

To measure the ring deposition after drying of the sessile droplet, two different pieces of equipment are used. The Wyko NT1100 Optical Profiling System is used to measure the shape of the whole ring deposition from suspensions of non-coated particles. Suspensions of coated polystyrene particles deposit in thin film layers and a finer resolution is needed to measure the deposition ring. For this purpose, the OLS4000 laser confocal microscope from Olympus is used.

3.3 Numerical approach

As we discussed in Chapter 2, the basic evaporation models solve the Laplace equation assuming a quasi-steady state, isothermal diffusion controlled evaporation for a fully pinned droplet. We will show in Chapter 4 and Chapter 6 that this produces a significant error for sessile droplets with a small initial radius $R < 500$ µm.

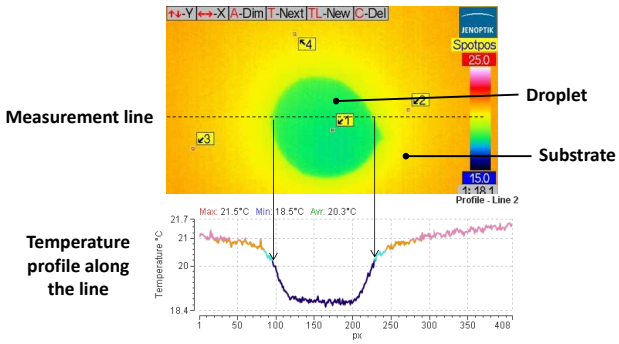

Figure 3.5: Temperature measurement of the surface of the droplet using an IR camera. During evaporation at room temperature, the enthalpy of the liquid near the surface reduces to transform liquid molecules into the vapor phase. That causes a drop of the temperature at the surface of the droplet during evaporation.

Hence, we use a numerical approach that solves the full energy equation for a locally averaged temperature. The model is developed based on custom FLOW-3D sub-routines (version 10.0.1, Flow Science, Inc., Santa Fe, NM 87505, United States). FLOW-3D is a computational fluid dynamics software that defines multi-physics flow problems by creating separate sub-routines representing each physics model. The sub-routines default equations can be customized and new parameters or equations can be added to each model through custom a code. To model the evaporation of a sessile droplet, we activate the *phase change*, *surface tension*, *heat transfer*, *viscous flow* and *residue deposition* physics models.

In the phase change physics module in FLOW-3D, the inertia of the gas adjacent to the liquid is assumed negligible. This approach has the advantage of reducing the computational effort as in most cases the details of the gas motion are unimportant for the motion of the much heavier liquid. Thus, the free surface becomes one of the external boundaries of the fluid region. A proper definition of the boundary conditions at the free surface then becomes important to achieve an accurate capture of the free-surface dynamics. To model the phase change at the fluid-air interface, instead of solving the diffusion equation, a local vapor density and velocity

of the molecules at the surface of the droplet define the local evaporation flux

$$\dot{m}_{local} = \alpha\sqrt{\frac{M}{2\pi\mathscr{R}\bar{T}}}(P_v - P_{air}), \tag{3.1}$$

where M is the molecular weight of a vapor molecule, $\mathscr{R}$ is the vapor gas constant, P_v and P_{air} are respectively saturation and air pressure, $\bar{T}$ is the local average of the liquid temperature along the surface and α is an accommodation coefficient that describes the probability of a vapor molecule at the liquid surface being detached from the surface. This accommodation coefficient is considered to be a function of the phase properties and is derived from experiments. The value of the phase change accommodation coefficient α is typically in the range of 0.001 to 0.1. We assumed a vaporization at the free surface of a fluid (droplet) at a constant saturation state defined by a void region (ambient air). The diffusion at the interface defines the rate limiting step of the evaporation while heat and mass transfer may occur between the liquid and the surrounding liquid (void region) and the solid surfaces. The vapor pressure in Equation 3.1 is then computed as a function of the local fluid temperature using a user-defined saturation curve. A Clausius-Clapeyron relation was used to find the vapor pressure P_v versus the temperature $T_{interface}$:

$$P_v = c_1 e^{\left(-\frac{\mathscr{L}}{\mathscr{R}T_{interface}}\right)} \tag{3.2}$$

where $\mathscr{L}$ is the latent heat of vaporization and c_1 is a constant of the vapor. While the pressure (P_a) and temperature ($T_{ambient}$) of the void is considered constant, $T_{interface}$ can be different than $T_{ambient}$ allowing heat transfer across the interface. The evaporation parameters in Equation 3.2 for evaporation of water molecules at room temperature are shown in Table 3.1.

For the heat transfer between fluid and air with the substrate, a first order internal energy advection is assumed and the energy equation is solved for each phase. Viscous-heating as a result of evaporation-induced flow is considered negligible. We also assume this internal flow to be laminar.

To model the surface tension effect, the initial contact angle of the droplet is defined from Equation 6.1. A linear variation of interfacial tension with temperature

Table 3.1: Coefficients for pressure and temperature at the interface in Equation 3.2.

Parameter	Value (CGS)
c_1	31690
$\mathscr{L}$	2.4423×10^{10}
$\mathscr{R}$	8.3145×10^{7}

was considered (i.e. $\mathrm{d}\sigma_{FG}/\mathrm{d}T$ was constant) so that the thermal Marangoni flow can be modeled. For the behavior of the contact line, we use a model that includes both pinned and de-pinned stages during the evaporation of colloidal suspensions. In the model, we define a receding contact angle, θ_r, that is determined from experiments. The behavior of the droplet then is considered to be in two different phases:

1. When the contact angle is above θ_r the velocity of the fluid at the contact line is zero and the contact area of the droplet is constant (pinned stage).

2. When the contact line reached θ_r, the contact line moved while keeping the contact angle constant (de-pinned stage).

To pin the contact line when the contact angle is above θ_r, we customize the surface tension model by creating a phantom obstacle that is attached to the contact line to keep the contact line pinned. This is achieved by creating a sub-component around the droplet that limits the spreading of the fluid and then assigning a wetting contact angle inside this region. The phantom sub-component basically sets the velocities inside the sub-component to zero so no fluid can enter. Also, the phantom sub-component does not have surface area so it does not interact with the surface tension model equations.

To model the deposition of the particles, we assumed non-cohesive particles that neither do interact with the flow nor with each other. The mass flow rate of a scalar entering the domain was then equal to the specified particle concentration times volume flow rate of the source fluid at the source. During the evaporation, the particle concentration will automatically be increased by removing fluid at the free surface of the fluid. If a surface element is less than half filled with liquid, then the concentration of the scalar will also occur in the principal neighbor of the

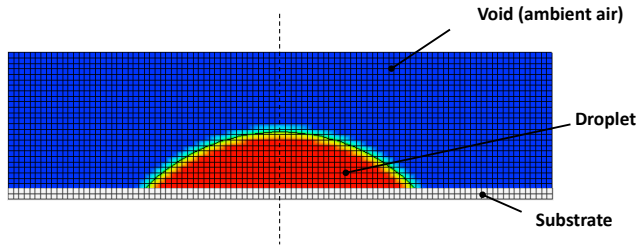

Figure 3.6: The schematic of the mesh structure using FAVOR technique in FLOW-3D.

surface element to the extent that the concentration change is spread over a region equal to half the thickness of the surface element. To find the deposition profile, the residue model in FLOW-3D was activated by setting a parameter defining a critical concentration for the particles, $C_{critical}$. Once the suspension is concentrated to its critical concentration near a solid surface, then any further concentration results in a residue on the substrate that is fixed (not moving).

The geometry was constructed using the Fractional Area/Volume Obstacle Representation (FAVOR) technique. In this method, the open area fraction inside a cell is computed along with the open volume fraction for a fixed mesh and then the fluid geometry is constructed based on the volume fraction information from cells (shown in Figure 3.6). This approach offers a simple and accurate way to represent free surfaces in the domain without requiring a body-fitted grid. Evaporation may take place only in cells containing a free surface. All temperatures are initially in equilibrium and equal to room temperature. Simulations are run for the maximum time step sizes of 2×10^{-5}, 1×10^{-5} and 1×10^{-6} seconds and maximum temperature differences between the fluid and air during the evaporation are consistent with 2% error. We use structured rectangular grids for the FAVOR to improve the accuracy and the stability of the numerical solutions. The rectangular grids with the sizes of 4 µm, 2 µm and 1 µm are used and the mesh dependency of less than 1% is observed for the maximum phase change rate and 0.5% for the maximum temperature differences. The time step size in our simulation is controlled by the convergence and the stability. The convergence of the solution was controlled by

Table 3.2: The safety factor coefficient for each physics module to ensure numerical stability.

Parameter	Value
ε_f	0.45
ε_s	0.5
ε_p	1
ε_h	0.45

setting the implicit iteration method for each solver and with the maximum number of iteration counts of 500. The numerical stability is checked by two criteria:

1. There should be no flow across more than one computational cell in one time step. This is checked by setting the coefficient ε_f so that:

$$\text{time step} < \varepsilon_f \cdot \min\left[\frac{\delta_r}{v_r}, \frac{\delta_z}{v_z}\right] \tag{3.3}$$

   where δ_r and δ_z are the rectangular cell sizes in r and z direction. When other modules exist in the model, additional coefficients of ε_s, ε_p and ε_h are used to account for the instability caused by surface tensions, phase change and heat transfer, respectively. The value of these coefficients in our simulation is mentioned in Table 3.2.

2. A cell with a large free surface area and a small volume could restrict the time step to small values if there is significant flow in this cell. This is automatically checked by an algorithm in FLOW-3D through monitoring the mesh locations and controlling the time step.

Chapter 4

Effect of substrate conductivity on the evaporation of small sessile droplets

4.1 Introduction

Sessile droplets are liquid drops that are located on top of a substrate surface. The evaporation of sessile droplets on substrates has been widely discussed in the literature due to the wide occurrence of this phenomenon in a variety of applications including inkjet printing [33], wetting [7], deposition processes [34] and bio assays [35]. In recent work the hydrodynamic flow generated during the evaporation of such droplets has been used to place and align nano particles, e.g. carbon nano tubes (CNTs) and nano wires [33]. Hence the understanding of the evaporation process of sessile droplets and investigating the important parameters affecting the evaporation process and flow dynamics is important for such applications.

During the evaporation of small sessile droplets on a surface, the contact line of the droplet undergoes two different stages: the pinned stage, with a fixed contact line, and the de-pinned stage with a moving contact line [1]. Figure 4.1 shows the contact angle and the radius of a water droplet measured over time, indicating these two stages. When the contact line is pinned, evaporation reduces the fluid volume

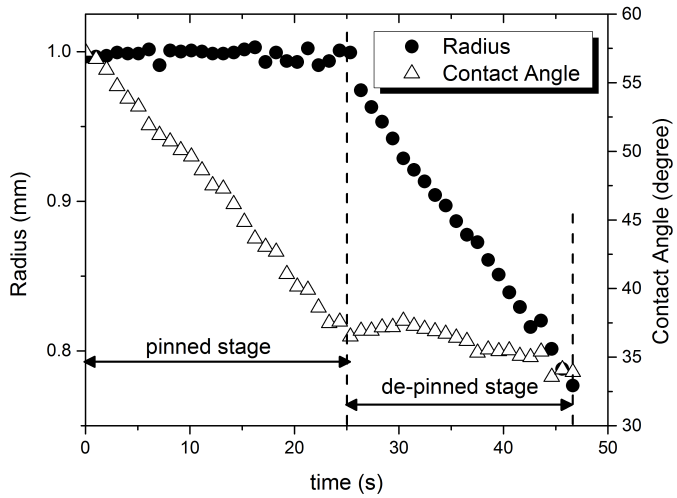

Figure 4.1: The radius and contact angle of a water droplet on an acrylic coated plastic slide during evaporation as a function of time showing two modes of evaporation, at 25°C and relative humidity of 55%.

at a constant footprint, leading to a reducing contact angle of the droplet (pinned stage). When the contact line reaches a certain contact angle, usually called a receding contact angle, θ_r, the contact line starts to move while the contact angle remains almost constant (de-pinned stage). The behavior of the contact line during each stage affects the hydrodynamic flow inside the droplets [20]. The evaporation flux of a sessile droplet in air is controlled by the rate at which the thin vapor layer above the surface diffuses into the ambient air [19]. It can be shown that the diffusion of the vapor into the ambient air is slow and it can be considered as a quasi-steady state.

Hu and Larson [19] suggested a basic model for diffusion, solved the Laplace equation of mass transfer with this assumption, and derived an equation for the evaporation flux at the surface of the droplet. In their model, they treated the local temperature gradient across the fluid due to latent heat of evaporation as negligible and solved the mass transfer equations at constant temperature, i.e. ambient temperature. This, combined with neglecting the effect of this local temperature gradient on vapor saturation concentration, leads to neglecting the effect of substrate conductivity; one would expect that heat from a substrate with a high thermal con-

ductivity can reduce the effect of fluid cooling caused by evaporation.
Popov [20] also used the assumption of a constant temperature and developed a basic model and found that the term for the evaporation rate divided by the droplet's initial radius

$$\frac{-\left(\frac{dV}{dt}\right)}{R_0} \approx \frac{4DC_v(1-\phi)}{\rho} \tag{4.1}$$

is independent of the droplet shape and is only a function of the phase change properties with the initial radius R_0, volume V, time t, vapor saturation concentration C_v, the diffusion coefficient of water vapor in air D, the ambient humidity of the vapor ϕ and the density of the fluid ρ.
While this basic model showed good agreement with droplets with a diameter of 1 mm and above, there was a considerable error for small droplets [19]. Dunn et al. [36] showed the strong influence of the substrate conductivity and droplet cooling on the evaporation and tried to improve the basic model by considering Newton's law of cooling and inserting the effect of buoyancy of the vapor in the atmosphere. Although their model was in good qualitative agreement, it under-predicts the experimental results. Here we present a model that includes the thermal effects of the phase change by adopting the cavity-liquid model presented by Plesset and Prosperetti [37]. Also in the basic model, it is assumed that the contact line is always remaining pinned. That could produce a significant error when a considerable time of the evaporation process occurs in the de-pinning stage (Figure 4.1). In our model, the movement of the contact line is included so that it matches the experimental results.

4.2 Numerical model

The numerical simulation is performed using the software Flow-3D (version 10.0.1, Flow Science, Inc., Santa Fe, NM 87505, United States). It solves the Navier-Stokes equation for the fluid, the energy equation for the fluid, the ambient air and the substrate, and solves the phase change equation for the air-liquid interface based on the cavity-liquid model presented in [37]. The schematic of the problem is shown in Figure 2.5. The no-slip boundary condition was used on the substrate surface and the movement of the contact line is following the concept that

was explained earlier in Figure 4.1). All temperatures are initially at equilibrium and equal to room temperature.

4.3 Materials

We used a Theta Lite optical tensiometer to measure the contact angle and radius of the droplet during the evaporation. Images were taken at 1 Hz. To print the droplets on the surface we used a MicroFab MJ-ABP-01 dispensing nozzle with the diameter of 80 µm. To show the effect of the substrate cooling on evaporation of small droplets, we chose four different substrates with different thermal conductivities: Copper (Cu) with $K = 400$ W/mK, glass with $K = 1.05$ W/mK, treated polystyrene coated plastic slides (Plastic Y) with $K = 0.03$ W/mK and treated UVT acrylic coated plastic slides (Plastic B) with $K = 0.02$ W/mK and printed the same volume of distilled water on them.

4.4 Results

Figure 4.2 shows the initial contact angle and radius of the 45 nL sessile water droplets printed on each substrate. For all of the substrates, a combination of the pinning and de-pinning was observed during the evaporation, similar to Figure 4.1. The volume of the droplets during the evaporation is shown in Figure 4.3. The total evaporation of the droplet, t_f, was defined as the time-intercept of the linear line, fitted to the data of droplet volume over time and the average evaporation rate was defined as the slope of this line.

The measured evaporation time of water droplets deviate consistently from the higher values predicted by the basic model [20], and the gap is particularly high for more thermally conductive substrates, i.e. Cu and glass, as shown in Figure 4.4. To investigate whether this discrepancy in the evaporation rate is related to thermal effects, the evaporation rate from the Popov model (Equation 4.1) which is independent of the shape of the droplet was compared with experiments (Figure 4.5). The basic model predicts the same value for all substrates and depends only on vapor diffusivity into the ambient air.

To show the effect of substrate cooling, the numerical simulation based on the model for diffusion described earlier (Equation 3.1) was developed. Substrates at

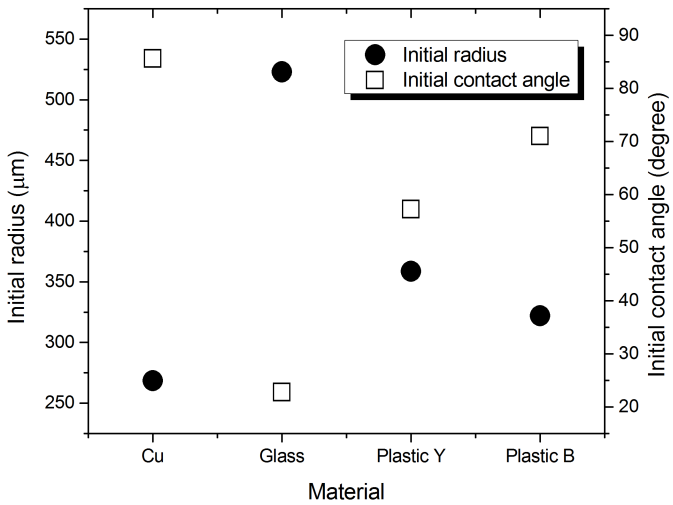

Figure 4.2: The contact angle and initial radius of water droplets on Cu, glass and plastic slides. All the measurements were within a margin of error of less than 2%.

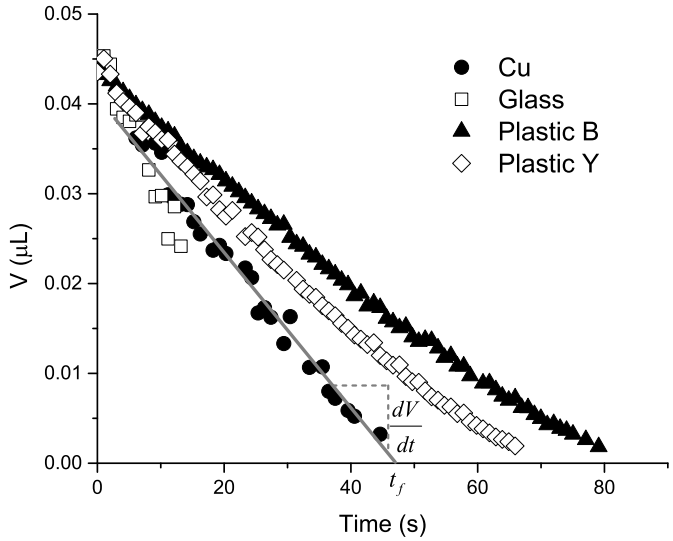

Figure 4.3: Droplet volume over time for different substrates.

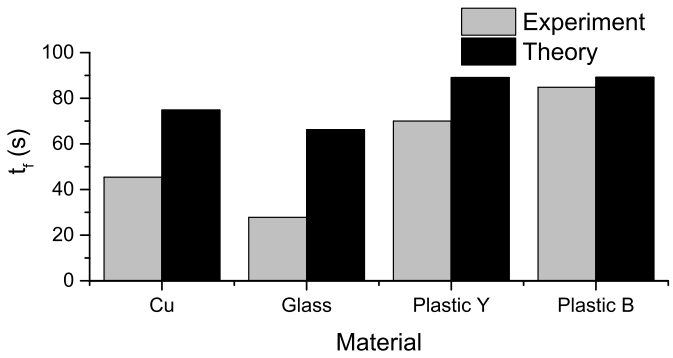

Figure 4.4: Total evaporation time, as measured by experiments (gray) and as predicted by the Popov model (black).

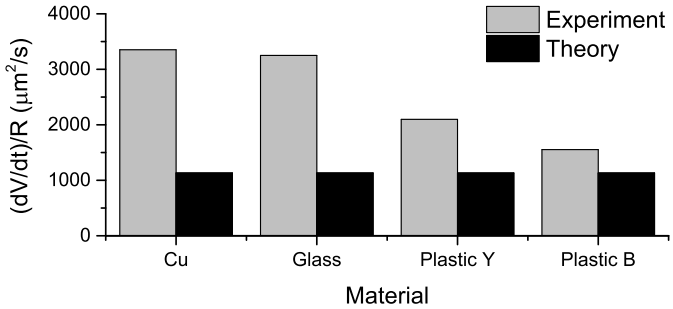

Figure 4.5: Comparing the measured evaporation rates with the values from the basic model from Equation 4.1.

different thermal conductivities were chosen and a water droplet with a fixed initial radius and contact angle was modeled. During the evaporation, the more conductive substrate was able to supply heat to the droplet, increasing the evaporation rate. Figure 4.6 shows the plot of the temperature inside the substrate for a substrate with the thermal conductivity of $K = 100$ W/(mK). Since the simulated droplets have the same initial geometry, the only parameter that could produce the difference in evaporation rate should be the thermal effects. The effect of the substrate cooling on evaporation rate is shown in Figure 4.7 by comparing the numerical simulation results with experiments and theory.

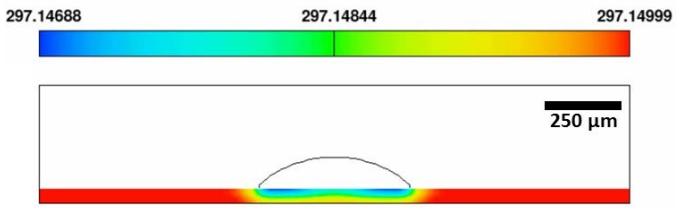

Figure 4.6: Temperature contours inside the substrate adjacent to the droplet

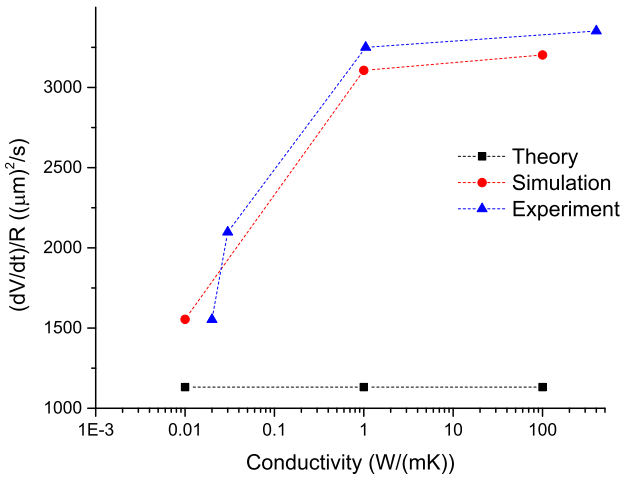

Figure 4.7: The effect of substrate cooling on the evaporation rate, the basic model shows the same value for all substrates.

4.5 Discussion

The results show the effect of substrate cooling on the evaporation of small droplets at room temperature. Previously Hu and Larson [19] showed that using the basic model for diffusion leads to a considerable error for small droplets less than 1 mm in diameter. To investigate the influence of substrate conductivity for small droplets, we consider a droplet with initial radius R_0 on a substrate as shown in Figure 2.5. The total amount of heat necessary for evaporation can be calculated by multiplying the latent heat of evaporation, $\mathscr{L}$ by the evaporation flux

$$\dot{Q} = \mathscr{L}\dot{m}, \tag{4.2}$$

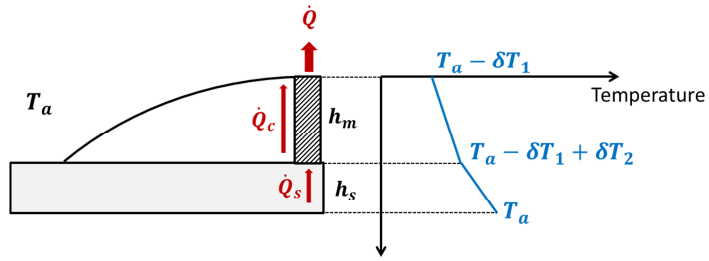

Figure 4.8: The schematic of the heat transfer through an element across the droplet.

where the evaporation flux, $\dot{m}$ can be approximated as [19]

$$\dot{m} \cong 2\pi D(1-\phi)C_v R_0. \tag{4.3}$$

This means that the total heat needed at the droplet surface for evaporation is linearly proportional to the size of the droplet. The molecules at the surface of the droplet get this amount of heat from the droplet itself. The droplet could either provide the entire amount while its enthalpy decreases in an infinitesimal time step, or could get part of this energy from the substrate, via substrate cooling. Figure 4.8 shows the heat transfer through an infinitesimal element across the droplet.
The balance of energy for the element yields

$$\dot{Q} - \dot{Q}_c = Ah\rho c_p \frac{\partial \bar{T}}{\partial t} \tag{4.4}$$

where $\bar{T}$ is the average temperature along h_m and $\dot{Q}_c$ is the heat conducted through the droplets from the fluid-substrate interface toward the surface of the droplet and is found as:

$$\dot{Q}_c = K_\ell A \left.\frac{\partial T}{\partial z}\right|_{z=0}, \tag{4.5}$$

where K_ℓ is thermal conductivity of the fluid. The temperature distribution inside the droplet can be found by solving the partial differential equation

$$K_\ell A \left.\frac{\partial T}{\partial z}\right|_{z=0} + Ah\rho c_p \left.\frac{\partial \bar{T}}{\partial t}\right|_{z=h_m} = 2D(1-\phi)c_v R_0 \mathscr{L}. \tag{4.6}$$

To simplify the problem, we assume the temperature change inside the volume element happens as the superposition of two separate temperature changes due to thermal capacity and conductivity. We assume first that the temperature of the droplet is decreasing steadily and that the droplet loses heat similarly to a lump body by the amount of δT_1. At the same time, the droplet uses the heat through conduction to increase its temperature by the maximum amount of δT_2 at the substrate-fluid interface. This amount of heat could be entirely obtained through the substrate conductivity (full substrate-fluid coupling) or the droplet itself (insulated substrate-fluid boundary). Therefore the temperature inside the element across the droplet yields to a profile shown in Figure 4.8.

The heat conducted through the droplet is helping the droplet to provide the amount of heat required for faster evaporation. If there is a full thermal coupling between the substrate and the fluid, i.e. the same temperature of the fluid and substrate at the fluid-substrate interface,

$$\dot{Q}_s = K_s A \left.\frac{\partial T}{\partial h}\right|_{substrate} = K_s A \frac{\delta T_1 - \delta T_2}{h_s}, \tag{4.7}$$

where K_s is thermal conductivity of the substrate. This shows that, in case of full thermal coupling of substrate-fluid, more heat can be provided through substrate conductivity when $(\delta T_1 - \delta T_2)$ is higher. From equation 4.5 and 4.7 and assuming that all of the conductivity heat is obtained from the substrate, we will have:

$$K_\ell \frac{\delta T_2}{h_m} = K_s \frac{\delta T_1 - \delta T_2}{h_s}, \tag{4.8}$$

or

$$\delta T_2 = \delta T_1 \left(1 + \frac{K_\ell h_s}{K_s h_m}\right)^{-1}. \tag{4.9}$$

We can write the scale of the height of the droplet for small droplet as:

$$h_m = R_0 \tan\left(\frac{\theta}{2}\right), \tag{4.10}$$

and combine this with Equation 4.9 to write it versus droplet radius:

$$\delta T_2 = \delta T_1 \left(1 + \frac{K_\ell h_s}{K_s R_0 \tan\left(\frac{\theta}{2}\right)}\right)^{-1}. \tag{4.11}$$

If we assume a constant thermal capacity at a certain height of the element shown in Figure 4.8, there will be an upper bound for the value of δT_1. Then we can see from Equation 4.8 that the value of $(\delta T_1 - \delta T_2)$ is higher at lower droplet radii

$$\delta T_1 - \delta T_2 = \delta T_2 \left(\frac{K_\ell h_s}{K_s R_0 \tan\left(\frac{\theta}{2}\right)}\right). \tag{4.12}$$

Hence, we conclude that when the size of the droplet shrinks, the influence of the substrate conductivity has a more important role for heat transfer into the system. Equation 4.12 suggests that in an infinitesimal time step with a full thermal coupling of substrate-fluid, heat transfer through the substrate to the droplet is easier when the conductivity of the substrate is higher. Moreover, from Equation 4.11 we could see that the effect of the droplet radius size is stronger when the value of

$$\left(\frac{K_\ell h_s}{K_s R_0 \tan\left(\frac{\theta}{2}\right)}\right) \gg 1, \tag{4.13}$$

or

$$R_0 \tan\left(\frac{\theta}{2}\right) \ll \left(\frac{K_\ell h_s}{K_s}\right). \tag{4.14}$$

The initial contact angle is defined by the interfacial forces balance on the contact line and by assuming that is independent of the radius size, we can find the critical radius of the droplet that below which the substrate cooling effect influences the evaporation time

$$R_0 \ll \left(\frac{K_\ell h_s}{K_s \tan\left(\frac{\theta}{2}\right)}\right). \tag{4.15}$$

where θ is the initial contact angle of the droplet before evaporation starts as shown in Figure 4.2.

4.6 Conclusions

Our experimental data shows that the substrate conductivity plays an important role in the evaporation of small sessile droplets. Although the temperature difference across a small droplet is not large, the substrate conductivity becomes important. We developed a numerical model (details in Section 3.3) to include the effect of the thermal conductivity of the substrate. Our numerical model is in good agreement with experimental data and supports the measurement results. While the theory predicts the same evaporation rates for a sessile droplet on substrates with different thermal conductivities, our experimental measurements and numerical results show a higher evaporation rate for a substrate with a higher thermal conductivity. Moreover, the numerical and experimental results converge to the results predicted by the theory when the conductivity of the substrate is low. Finally, we discussed the substrate cooling effect of the droplet size and showed that for sessile droplets, below a critical radius the substrate conductivity becomes substantial.

Chapter 5

Evaporation of line droplets on a substrate

5.1 Introduction

The study of the evaporation of liquid droplets on a substrate is a classical fluid mechanic topic. When droplets are freely sitting on a substrate, the liquid molecules evaporate by transition into a vapor layer at the surface of the droplet. The evaporation rate is controlled by the transfer rate across the liquid-vapor boundary (kinetically-controlled evaporation) or the diffusive relaxation of the saturated vapor layer (diffusion-controlled evaporation) [18, 19]. The droplet shape will change during the evaporation, depending on whether the evaporation happens with a fixed contact line (pinned stage) or with a moving contact line (de-pinned stage) or a combination of both. Inside a so-called "point droplet" with a spherical cap, the evaporation with pinned contact line induces an internal flow toward the contact line of the droplet [25, 27]. In the evaporation of colloidal suspensions, this flow carries the solute particles to the corners leading to a deposition along the ring-shaped contact line and this phenomenon is often referred to as the "coffee-ring" effect [18, 27, 38].

For the evaporation of small droplets the effect of the gravitational forces is negligible and the shape of the droplet is defined by the balance of the interfacial forces between the solid, liquid, and gas phase. Therefore, the evaporation-induced flow

in small droplets is mainly governed by the interplay of these forces during the evaporation. This makes the evaporation process and hence the deposition of the solute particles more controllable [3]. There has recently been growing interest in deposition and transport processes at micro scales using the evaporation-induced flow in sessile droplets [3, 9, 11, 13–15]. Sharma et al. [3, 9] used this flow for the placement and alignment of carbon nanotubes with line droplets with a high aspect ratio of 1000:1 (length to width).

The micro flow induced by evaporation in small point droplets on a substrate has been extensively studied before. Deegan et al. [18] developed a method to describe the diffusion controlled evaporation and used this model to find the average flow velocity inside the droplet toward the contact line for small point droplets with a fully pinned contact line. Tarasevich [23] assumed potential flow inside the droplet and a uniform evaporation rate over its surface and analytically solved the flow field for fully pinned point droplets and found the velocity profile inside the droplet. Hu and Larson [27] solved the micro flow for a droplet with a fully pinned contact line and a small height using the Navier-Stokes equation. Fischer [39] used lubrication theory to solve for the particle convection in an evaporation-induced flow with either fully pinned or fully de-pinned contact lines. Popov [20] solved the momentum and mass equations locally and globally for fluid and solute particles and developed a closed-form expression for particles deposition at the contact line as a result of evaporation-induced flow. While an extensive study of point droplets exists in the literature, the evaporation of droplets with other shapes including line droplets is a rather untouched area.

Line droplets of different aspect ratios are usually produced at a small scale by using micro contact [3, 9] or inkjet printing methods [40–44]. The shape of line droplets of small size, when the magnitude of gravity is negligible, is mainly defined by the interplay of the interfacial tension forces, similar to point droplets. However the behavior of the contact lines at the long sides and at the ends of a line droplet is not necessarily the same. This introduces a higher level of complexity to the evaporation process. Particularly, unlike point droplets, it is possible for line droplets to have simultaneously pinned contact lines at the sides and de-pinned contact lines at the ends during the evaporation. Petsi and Burganos solved the potential flow for infinite line droplets of cylindrical shape by assuming that all the

contact lines at the sides and at the ends are pinned during the evaporation [24]. They continued their study and solved the Stokes flow for any contact angle [25] when all contact lines are anchored. Masoud and Felske [26] solved the Stokes equation for infinite line droplets with both fully pinned or fully de-pinned side contact lines. However, to the best of our knowledge, there is no work in the literature discussing droplets with finite ratio of length to width and there is no model that explains the different behaviour of the side and end contact lines during the evaporation of line droplets. All of the models that assume infinite line droplets ignore the line ends. However, relatively high evaporation rates occur at the ends and it is likely for the droplet to shrink primarily from the ends. In fact, the models for infinite line droplets correspond to models for point droplets with a slightly different evaporation rate distribution at the surface of the droplet.

Here we develop a model that considers the effect of both side and end contact lines using energy methods, and we solve for the evaporation rate distribution and the velocity field in 3D.

5.2 Model development

When a line droplet is printed on a substrate, the elongated droplet readily assumes the same contact angle θ everywhere. The shape of the line droplet consist of a cylindrical segment with the length L at the center connected to two spherical caps at both ends with the initial radius R of their footprint (Figure 5.1).

Similar to the spherical droplet, at any given contact angle θ, of the line droplet, the geometry of the droplet results in a non-uniform evaporation flux at the surface. For non-rotationally symmetrical geometries such as line droplets, this leads to a complex contact line behavior at the different locations around the droplet which leads to complex flows inside the droplet.

We first develop a model that describes the geometry of the droplet during evaporation, including a discussion of the contact line behavior, using an energy minimization approach (Section 5.2.1). Then, given the geometry of the droplet for a given remaining fluid volume, we find the evaporation rate distribution assuming a quasi-steady state regime and diffusion controlled evaporation. Finally, we use the

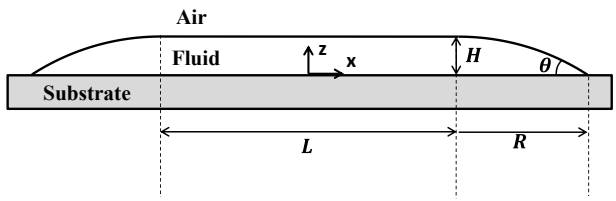

(a) Side-view

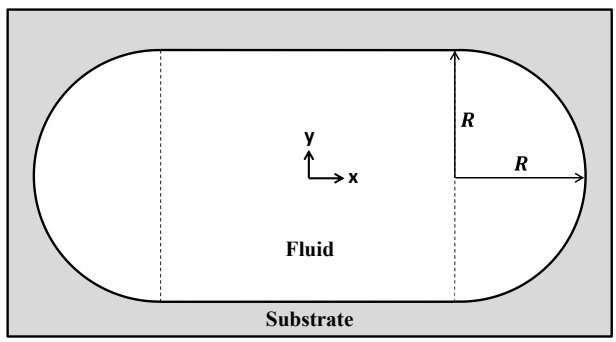

(b) Top-view

Figure 5.1: Line droplet from (a) side-view and (b) top-view

potential flow assumption to approximate the evaporation induced flow inside the line droplet (Section 5.2.2).

5.2.1 Contact line behavior

Under the assumption that the interior flow occurs on a much shorter time scale than the evaporation [27], the shape of the droplet will be determined by minimizing the energy associated with interfacial tension at a given volume [45, 46]. Our basic model will consider a droplet of a given volume deposited on a substrate with interfacial tensions for the liquid-gas, liquid-substrate and substrate-gas interfaces. This global approach is equivalent to a local equilibrium where forces on the triple point between the liquid, gas and substrate are considered, but it will be more convenient for less symmetric shapes.

However this basic model does not allow for the often experimentally observed

hysteresis where the contact angle at the triple point differs for an advancing and a receding contact line. This behavior can be described by introducing an additional property, different surface tensions for wetted and un-wetted substrate . When the contact line is advancing, the droplet will be covering un-wetted substrate, but when the contact line recedes it uncovers wetted substrate. This difference in surface energy will change the balance of forces at the triple point and will result in a difference between the advancing and receding contact angle.

This approach can be demonstrated with the well understood case of a droplet with a circular footprint. The minimum area surface with this footprint is a spherical cap that is described by two parameters, the radius of the footprint and the contact angle. Fix the zero point of the energy by setting the surface tension of the un-wetted substrate-gas interface to vanish. Then denote the surface tensions for the liquid-gas, liquid-substrate, wetted substrate-gas and un-wetted substrate-gas interfaces by σ_{FG}, σ_{SF}, $\sigma_{SG,d}$, and $\sigma_{SG,w}$ respectively. Then the energy of a droplet with a circular footprint of radius R and a contact angle θ deposited onto an un-wetted substrate can be easily calculated as

$$E = \sigma_{FG} A_{cap}(R,\theta) + \sigma_{SF} A_{footprint}(R) \tag{5.1}$$

where

$$A_{cap}(R,\theta) = 2\pi R^2 \tan\left(\frac{\theta}{2}\right) \tag{5.2}$$

and

$$A_{footprint}(R) = \pi R^2. \tag{5.3}$$

This energy must be minimized under the constraint that the volume

$$V(R,\theta) = \frac{\pi R^3}{3\sin^3\theta}(2 - 3\cos\theta + \cos^3\theta) \tag{5.4}$$

be fixed to a given V_0. For this simple geometry, this minimization can be performed exactly and the contact angle is found to be independent of the size of the

droplet. This is the advancing contact angle,

$$\theta_A = \arccos\left(-\frac{\sigma_{SF}}{\sigma_{FG}}\right). \tag{5.5}$$

For an existing droplet which is receding, the interfacial tension of the wetted substrate becomes relevant. If R_0 is the initial radius of the footprint, the energy for a smaller droplet with footprint radius R is

$$E = \sigma_{FG} A_{cap}(R,\theta) + \sigma_{SF} A_{footprint}(R) + \sigma_{SG,w} A_{wetted}(R,R_0) \tag{5.6}$$

where

$$A_{wetted} = \pi R_0^2 - \pi R^2. \tag{5.7}$$

Again, for this simple geometry this minimization can be performed exactly and the contact angle is independent of the size of the droplet.This is the receding contact angle,

$$\theta_r = \arccos\left(-\frac{\sigma_{SF} - \sigma_{SG,w}}{\sigma_{FG}}\right). \tag{5.8}$$

Notice that as long as the droplet is receding, R_0 has no effect on its shape, as we can split its energy,

$$E(R,\theta,R_0) = E_{droplet}(R,\theta) + E_{wetsubstrate}(R_0), \tag{5.9}$$

into a term that depends only on the current shape of the droplet,

$$E_{droplet}(R,\theta) = \sigma_{FG} A_{cap}(R,\theta) + (\sigma_{SF} - \sigma_{SG}) A_{footprint}(R), \tag{5.10}$$

and a term with depends only on R_0,

$$E_{wetsubstrate}(R_0) = \sigma_{SG,w} A_{footprint}(R_0). \tag{5.11}$$

The only effect of the wetted substrate is to change the effective liquid-substrate surface tension for a receding droplet from σ_{SF} to $\sigma_{SF} - \sigma_{SG}$. This means that the region of the wetted substrate can recede with the contact line of the droplet with-

out affecting the droplet shape.

This model includes the well-known phenomenon of pinning. When a droplet is deposited onto un-wetted substrate, it will settle at the advancing contact angle. If a small amount of the liquid is removed, for example by evaporation, it will not be energetically favorable for the droplet to expose the wetted substrate and so the contact angle will decrease with a fixed footprint until it reaches the receding contact angle. This behavior can be verified by numerically minimizing the energy from Equation 5.6 in this intermediary regime.

The advantage of this energy formulation is that it can be easily extended to more complicated footprints, here to the elongated droplet shown in Figure 5.1b as a rectangle with circular ends.

Then the minimal surface covering a volume of liquid occupying this footprint will be a cylinder segment with spherical caps attached to the ends. This minimal surface has 3 parameters, R the radius of the circular part of the footprint or half the width of the rectangular part, L the length of the rectangular part and θ the contact angle. Because the surfaces attaching to the circular ends and the rectangular middle must match smoothly at their interface, the contact angle must be the same all along the liquid-gas-substrate triple point (the contact line) throughout the evaporation.

This 3 parameter minimization problem is tractable to numeric minimization:

$$\begin{aligned} E(R,L,\theta,R_0,L_0) = \sigma_{FG} A_{cap}(R,L,\theta) \\ + \sigma_{SF} A_{footprint}(R,L) \\ + \sigma_{SG,w} A_{wetted}(R,R_0,L,L_0), \end{aligned} \tag{5.12}$$

where L_0 is the initial length of the line droplet,

$$A_{cap}(R,L,\theta) = 2\pi R^2 \tan\left(\frac{\theta}{2}\right) + \frac{2RL\theta}{\sin\theta}, \tag{5.13}$$

$$A_{footprint}(R,L) = \pi R^2 + 2LR, \tag{5.14}$$

and

$$A_{wetted}(R,R_0,L,L_0) = A_{footprint}(R_0,L_0) - A_{footprint}(R,L). \tag{5.15}$$

This energy must be minimized under the constraint that the volume of the line droplet

$$V(R,L,\theta) = \frac{\pi R^3}{3\sin^3\theta}\left(2-3\cos\theta+\cos^3\theta\right) + \frac{LR^2}{2\sin^2\theta}\left(2\theta-\sin(2\theta)\right) \tag{5.16}$$

is fixed to a given V_0.

When numerically solving this problem, multiple stages of the evaporation can be seen. First there is a fully pinned stage, where the footprint is fixed and the contact angle decreases. Next there is a partially pinned stage where L and θ decrease but R is fixed, until L vanishes. Finally there is the fully de-pinned stage when θ is fixed and R decreases.

Informed by these numerical results, the partially pinned stage can be studied by fixing R. This reduces the problem to a two parameter minimization which can be solved analytically. We find that:

$$\frac{L}{R} = \frac{f(\theta,(\sigma_{SF}-\sigma_{SG,w})/\sigma_{FG})}{g(\theta,(\sigma_{SF}-\sigma_{SG,w})/\sigma_{FG})} \tag{5.17}$$

where f and g are functions of the contact angle and interfacial tensions and are equal to

$$f(\theta,(\sigma_{SF}-\sigma_{SG,w})/\sigma_{FG}) = \pi\left(\cos\theta+(\sigma_{SF}-\sigma_{SG,w})/\sigma_{FG}\right)(1-\cos\theta)^2 \tag{5.18}$$

and

$$\begin{aligned} g(\theta,(\sigma_{SF}-\sigma_{SG,w})/\sigma_{FG}) = {} & \theta^2\cos\theta \\ & -\theta\sin\theta\left(\sin\theta-2\left(\sigma_{SF}-\sigma_{SG,w}\right)/\sigma_{FG}\cos\theta\right) \\ & -\sin^2\theta\left(\cos\theta+2\left(\sigma_{SF}-\sigma_{SG,w}\right)/\sigma_{FG}\right). \end{aligned} \tag{5.19}$$

When L vanishes,

$$\cos\theta = -\left(\sigma_{SF}-\sigma_{SG,w}\right)/\sigma_{FG} = \cos\theta_r, \tag{5.20}$$

the receding contact angle for the point droplet. Thus the partially de-pinned stage transitions directly into the fully de-pinned stage of a point droplet when L reaches zero. The right hand side of Equation 5.17 has a divergence in theta for $\pi/4 \leq -(\sigma_{SF} - \sigma_{SG,w})/\sigma_{FG} \leq 1$, which moves from $\theta = \pi/2$ at the start of this range to $\theta = 0$ at the end. This means that within this range of parameters, this relation is invertible for an arbitrary aspect ratio and we can find a critical contact angle at which the partial depinning begins for any given aspect ratio.

To illustrate this, consider a given initial aspect ratio and contact angle. When the initial contact angle is higher than that given by the relation in Equation 5.17, then evaporation starts with a fully pinned stage at a fixed aspect ratio. Once the contact angle meets that given by the relation in Equation 5.17, the partially pinned stage begins where the contact angle decreases at the same time as the aspect ratio, while preserving this relation. Once L vanishes, the droplet will follow the fully de-pinned stage of the point droplet.

5.2.2 Velocity field

To calculate the flow field induced by evaporation, we first need to know the evaporation flux on the surface of the droplet. Assuming diffusion controlled evaporation and quasi-steady state diffusion, the evaporation flux is governed by the Laplace equation

$$\nabla^2 C = 0, \tag{5.21}$$

where C is the vapor concentration around the droplet [19]. The concentration outside the droplet is found by solving this equation with the following boundary conditions:

at $|x| \gg (R + L/2)$ or $z \gg H$ or $|y| \gg R$:

$$C = \phi\, C_v \tag{5.22}$$

where ϕ is the relative humidity and C_v is the saturated vapor concentration in air, at $z = 0$ there is no flux into the substrate

$$\nabla C = 0, \tag{5.23}$$

and at the surface of the droplet the concentration is equal to the vapor saturation concentration

$$C = C_v. \tag{5.24}$$

By knowing the concentration field, we can calculate the evaporation mass flux at any point on the surface of the droplet by

$$\vec{J}(x,y,z) = D\vec{\nabla}C, \tag{5.25}$$

where D is the diffusion coefficient of water vapor in air. Hence, we know the amount of fluid removed at the surface of the droplet and the geometry at each quasi-steady state time step. While in principle the flow could be rotational, the main flow behavior for relatively slow shape changes in this quasi-static case can be approximated by the potential flow formulation. For spherical droplets the velocity field and streamlines modeled by a potential flow matched well in magnitude and shape with Stokes flow and the Navier-Stokes solutions [23, 24, 26, 27]. Hence, since the evaporation-induced flow is in principle the same for droplets of any size and footprint shape, it makes sense to similarly assume that the potential flow describes the internal flow field for the quasi-static flow generated inside line droplets at good approximation. The potential flow field described by φ yields

$$\nabla^2\varphi = 0, \tag{5.26}$$

with the following boundary conditions:
Symmetry at $x = 0$:

$$\frac{\partial\varphi}{\partial x} = 0 \tag{5.27}$$

Symmetry at $y = 0$

$$\frac{\partial\varphi}{\partial y} = 0 \tag{5.28}$$

at $z = 0$ there is no flow through the substrate:

$$\frac{\partial\varphi}{\partial z} = 0 \tag{5.29}$$

the kinematic boundary condition at the surface of the droplet, the normal velocity is equal to:

$$\left(\vec{n}\cdot\frac{\partial\varphi}{\partial n}\right)=\frac{\vec{n}\cdot\vec{J}}{\rho}+[\vec{n}_x,\ \vec{n}_y,\ \vec{n}_z]\cdot\left[0,\ 0,\ \frac{\partial h}{\partial t}\right], \tag{5.30}$$

where ρ is the density of water, h is the local height of the droplet at any point, $\vec{n}$ is a unit vector along the normal direction to the surface, and n_x, n_y, and n_z are the x, y and z components of the unit vector n, respectively. If we assume that during the evaporation, the droplet shape remains a spherical cap at both ends with a cylindrical segment at the center, we can relate $(\partial h/\partial t)$ at any point of the droplet surface (x,y,z) to the liquid line height, H, using geometrical constraints

$$\begin{aligned}\frac{\partial h}{\partial t}=&\left(\frac{H^4-R^4}{4H^3\sqrt{\left(\frac{H^2+R^2}{2H}\right)^2-r^2}}+\frac{R^2+H^2}{2H^2}\right)\dot{H}\\&+\frac{r(x-\frac{L}{2})}{\sqrt{\left(\frac{H^2+R^2}{2H}\right)^2-r^2}}H(x-L/2)\dot{L}\\&+\left(\frac{R}{2H^2}\frac{H^2+R^2}{\sqrt{\left(\frac{H^2+R^2}{2H}\right)^2-r^2}}-\frac{R}{H}\right)\dot{R},\end{aligned} \tag{5.31}$$

where r is the $xy-$planar projection of the distance of this point from the center line of the cylindrical segment; this means $r=y$ for $|x|\leq L/2$ and $r^2=(x-L/2)^2+y^2$ for $x>L/2$.

5.3 Results

To investigate the flow field inside line droplets generated by evaporation at room temperature of $T=24°$C and relative humidity of $\phi=0.5$, we first choose a water line droplet on a glass substrate with an initial aspect ratio of $L_0/R_0=10$ and initial radius of $R_0=1$. Then we follow step by step the model that was presented

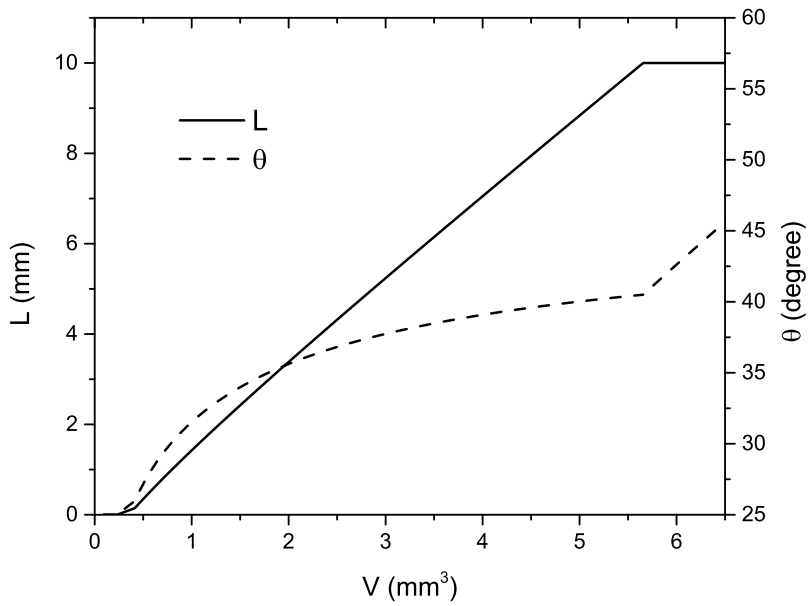

Figure 5.2: Length L and contact angle θ of a line droplet with the initial aspect ratio of $L_0/R_0 = 10$.

above for finding the velocity field. First, the contact angle θ and the length of the line droplet L are calculated from Equation 5.17 as the fluid volume is reduced by evaporation (Figure 5.2). The rate at which L and θ change with the fluid volume V is calculated by finding their derivatives $\mathrm{d}L/\mathrm{d}V$ and $\mathrm{d}\theta/\mathrm{d}V$ from Equation 5.17 as shown in Figure 5.3. The rate of change with respect to time, i.e. $\dot{L}$ and $\dot{\theta}$, is found by multiplying these values by the total evaporation rate from Equation 5.25. Then, the diffusion controlled evaporation is modeled by solving the Laplace equation. The local evaporation flux is calculated using Equation 5.25. The evaporation flux across the cylindrical and spherical parts is shown in Figure 5.4. The evaporation flux across the droplet along its length is obtained by Equation 5.25 and is shown in Figure 5.5. The total evaporation rate is found by integrating the local flux $\vec{J}(x,y,z)$ over the surface for each time step. Then the potential flow is solved with the boundary condition shown in Equations 5.27 to 5.30 (Figure 5.6).

Using the potential flow function, we can find the velocity field. As shown in Figure 6, the potential flow solution yields an outward velocity both along and across the

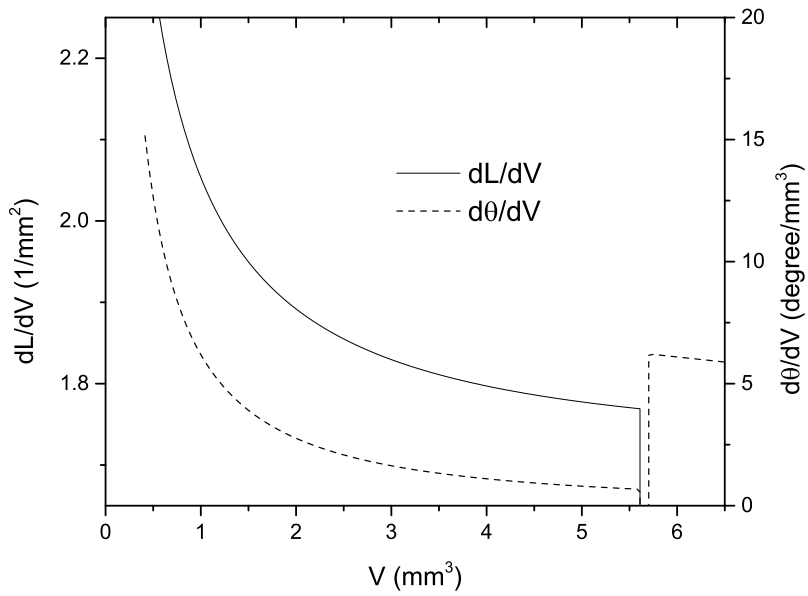

Figure 5.3: The change of the contact angle θ and the line length L with droplet volume for a shrinking droplet with an initial aspect ratio of $L_0/R_0 = 10$.

droplet with a higher magnitude along the length of the line droplet.

The quasi-steady state assumption dictated the outward velocity field pattern for line droplets with acute initial contact angles near the contact line for all aspect ratios L/R during the evaporation similar to the velocity field in Figure 5.7 for a line droplet with the initial aspect ratio of $L_0/R_0 = 10$. Equations 5.17 to 5.19 show that during the partially pinned stage of the evaporation, the contact angle θ depends only on the aspect ratio L/R of the droplet for given initial and receding contact angle parameters. The contact angle as the line droplet shrinks as a result of evaporation versus the aspect ratio of the droplet is shown in Figure 5.8, where is can be seen that for the partially pinned stage the aspect ratio and the contact angle follow a fixed relationship independent of the width of the droplet, $2R$ or the initial aspect ratio.

Finally, the effect of changing the interfacial tensions equivalent to changing the receding contact angle in the point droplet was studied for a droplet with $R_0 = 1$ mm and $L_0/R_0 = 10$ mm. Figure 5.9 shows the effect this has on the relationship

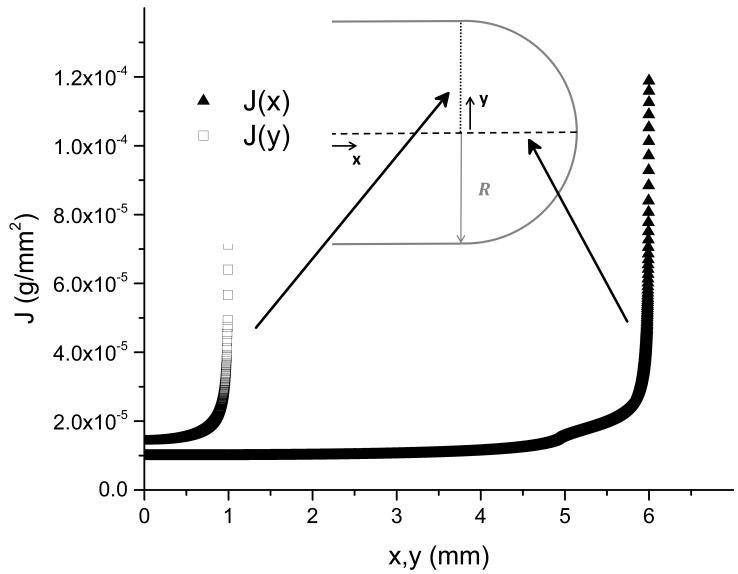

Figure 5.4: The evaporation flux on the centerline of the droplet and the spherical end for the droplet with the initial aspect ratio of $L_0/R_0 = 10$.

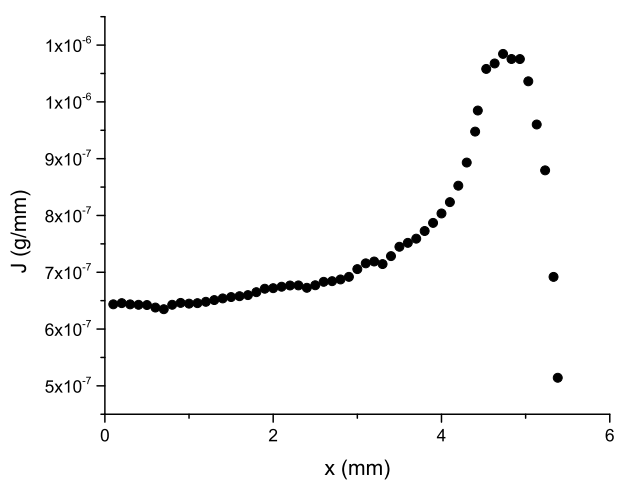

Figure 5.5: The evaporation flux across the line droplet of the shrinking droplet for an initial aspect ratio of $L_0/R_0 = 10$ at $L = 8.86$ mm.

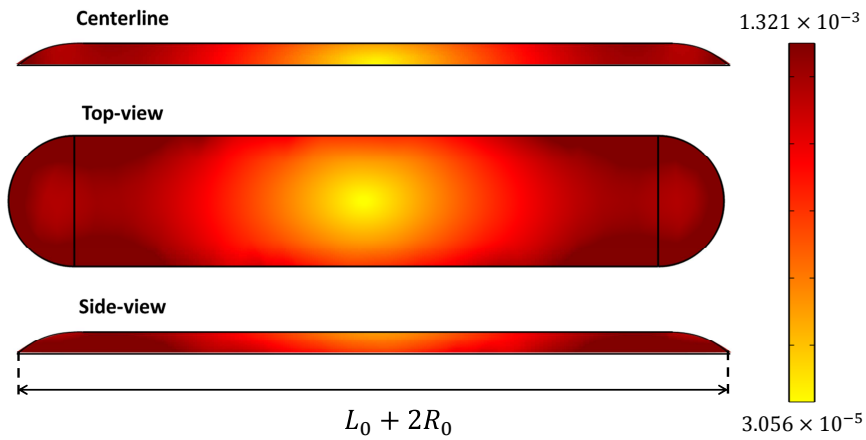

Figure 5.6: The contour plots of the evaporation induced flow magnitude in m/s in a line droplet with the initial aspect ratio of $L_0/R_0 = 10$.

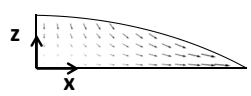

(a) The velocity field in *zx* plane

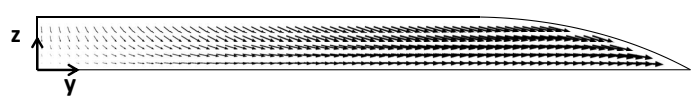

(b) The velocity field in *zy* plane

Figure 5.7: The outward velocity vectors across the droplet at (a) the *zx* plane and (b) *zy* plane. Cross sections are taken at the middle of the droplet.

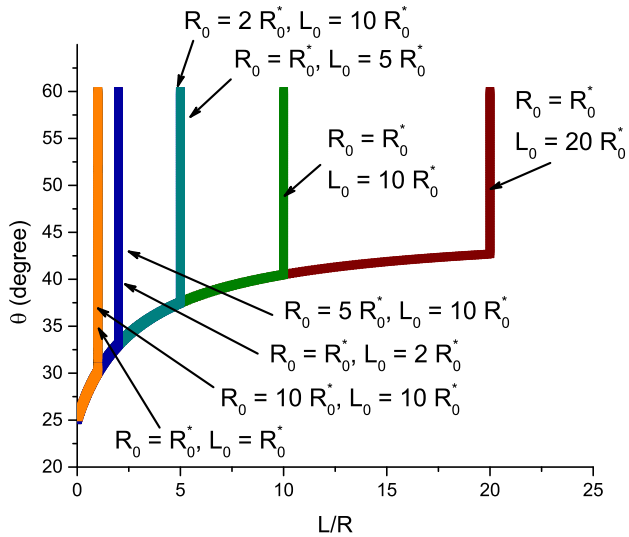

Figure 5.8: The contact angle versus the aspect ratio for the fully and partially pinned stages of the evaporation. The relationship between these two in the partially pinned stage can be seen to be independent of the initial aspect ratio and radius. The initial and receding contact angles are 60° and 20°, respectively.

between the contact angle and the aspect ratio during the partially pinned stage of the evaporation, for different receding contact angles.

5.4 Discussion

Our results show that the pinning of the contact line of line droplets leads to the outward evaporation-induced flow toward the contact line as previously described for spherical and infinite cylindrical droplets [24–27]. However, for the line droplets with aspect ratios of $L/R > 1$, the evaporation at the ends of the line is considerably higher compared to the center of the droplet (as shown in Figure 5.4). The higher evaporation rate requires more fluid to move toward these sites. Hence the outward flow toward the ends along the droplet is higher as shown in Figure 5.7. However this flow does not necessarily balance the high evaporation rate. In fact, in Figure 5.8 and Figure 5.9, we show that at the ends of the line droplet, the contact line starts to recede at a much higher contact angle compared to the receding contact

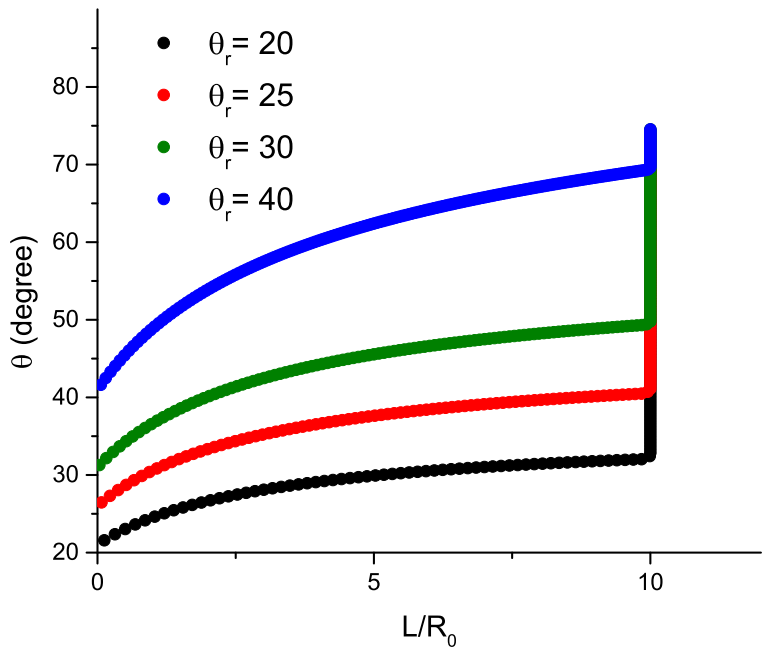

Figure 5.9: The contact angle as a function of aspect ratio in the partially pinned stage of line droplet evaporation for line droplets for different receding contact angles. R_0 and L_0 are fixed to 1 mm and 10 mm, respectively.

angle of spherical droplets. This higher receding contact angle occurs while the width of the droplet remains constant, but the length of the droplet shrinks. For higher aspect ratio droplets, the contact angle at which the ends start to recede is higher (as shown in Figure 5.8 and Figure 5.9) and the initial stage of a fully pinned contact line is consequently shorter. Therefore, the stronger flow toward the ends is opposed by the ends receding sooner for long droplets.

Also, we can see from Equations 5.17 to 5.19 and Figures 5.8 and 5.9 that the contact angle at which the two end caps of the line droplets join each other (i.e. when $L = 0$ and the footprint becomes circular) is the receding contact angle of the point droplet independent of the initial shape and initial equilibrium contact angle of the droplet. This is of course subject to the assumptions of our model that shows good agreement with the experimental results when applied to spherical droplets [47].

5.5 Conclusions

Here we explored a new method that models the evaporation of line droplets with different shapes and length to width ratios. Using a global method where the energy of interfacial tensions is minimized allows us to study more complicated droplet shapes in a straightforward manner. This method allows the de-coupling of the evaporation and momentum equations of the fluid and the contact line and hence could be used for any droplet shape. Our results show that during the evaporation of line droplets, while the equations for fluid momentum and evaporation are similar to spherical sessile droplets in principle, the complex behavior of the contact line in different regions of the droplet affects the evaporation-induced flow field inside the droplet. Our model uses a new approach to study the evaporation of line droplets and the evaporation rate and evaporation-induced flow results from our model need to be verified by experiments in future work.

In our method we used the potential flow assumption for simplicity and to show the main idea of the model. Including the viscous effects by solving the Navier-Stokes equations for the fluid would be an interesting direction for further investigation. However, this would result in a complex instability problem and the de-coupling of the contact line momentum equation from the fluid would be a challenge. Depending on the scale of the droplet geometry and interfacial forces, a discontinuity in the line droplet is expected. Surface roughness effects could also be added to the energy model in future work.

Chapter 6

Effect of surfactants and substrate temperature on contact line behavior

6.1 Introduction

As mentioned previously, the initial contact angle of a sessile droplet with the substrate surface is defined by the balance of the interfacial tension forces at the contact line of the droplet. During the evaporation of sessile droplets of colloidal suspensions, particles deposit along the contact line as a result of "coffee ring" effect [18]. This is caused by the evaporation-driven flow evaporation inside the droplet which carries the solute near the contact line [19, 27]. The deposition of solute using the evaporation induced flow inside droplets has applications in a variety of areas such as biology [10, 15, 48–50], separation processes [12], deposition processes [3, 6, 9] inkjet printing [4, 33, 41, 42, 51], and wetting processes [52–55].

The contact line motion during evaporation is the key to understanding the flow generated during the evaporation of sessile droplets [24–26]. For a hydrophilic substrate and a droplet with a fixed contact line an outward flow is generated inside the droplet, while a receding contact line results in an inward flow inside the droplet [26]. During the evaporation of sessile droplets two separate stages for the

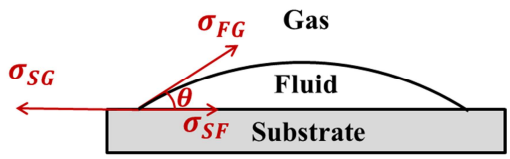

Figure 6.1: Interfacial forces on the contact line during the evaporation of a sessile droplet.

contact line behavior exist: evaporation with a fixed contact line (pinned stage) and evaporation with a moving contact line (de-pinned stage). During evaporation of a droplet, in general both stages exist, starting with the pinned contact line with reducing contact angle followed by the de-pinned stage with moving contact line and constant contact angle. The evaporation-induced flow for each stage has been determined separately and the flow dynamics have been discussed extensively [23–27]. Petsi and Burganos showed that for evaporation with constant evaporation flux (kinetically controlled evaporation) of the droplets with an initial contact angle of less than $\pi/2$, the pinned stage produces an outward flow while the de-pinned stage creates an inward liquid flow [25]. Masoud and Felske analytically solved the internal flow for droplets with diffusion controlled evaporation and showed that while the flow is always outward at any contact angle for droplets with a fully pinned contact line, the moving contact line creates a complex flow pattern including both flow toward and away from the contact line [26]. However, in all of these studies, only a single stage of the evaporation has been studied, not a combination of the stages. This is mainly due to the complexity that the transition from one stage to another imposes on the flow dynamics inside the droplet. This transition between the stages results from the balance of the interfacial forces at the contact line. The three effective forces on the contact line during the evaporation acting on the substrate-gas (σ_{SG}), substrate-fluid (σ_{SF}) and fluid-gas interfaces (σ_{FG}) are shown in Figure 6.1.

Assuming a homogeneous, rigid, isotropic solid substrate surface that is impermeable to fluid, and by neglecting the contribution of the droplet size on the equilibrium contact angle [56], we can write the Young's equation for the ideal three

phase systems as

$$\sigma_{SG} - \sigma_{SF} - \sigma_{FG} \cos\theta = 0, \tag{6.1}$$

where θ is the equilibrium contact angle. The adsorption of colloids or surfactant in colloidal suspensions in water at the fluid-gas interface or at the substrate-fluid interface, could alter the surface tension and consequently the contact angle [57–59]. Okubo et al. showed that while the diameter of the silica microspheres at $T = 24°$C has no major effect on the surface tension at the fluid-gas interface for a particle concentration within the range of 0.0001-0.02 wt%, the surface tension changes due to the presence of polystyrene particles when the microsphere diameter is smaller than 0.2 μm [59]. They related this phenomenon to the special ordering of the particles near the fluid-gas interface as a result of the strong hydrophobic surface of the polystyrene microspheres. However they reported that for particles larger than 0.2 μm in diameter the surface tension remains constant and equal to the value of the pure water at different particle concentrations up to 0.1 wt%. Hydrocarbon surfactants such as TWEEN®20 or sodium dodecyl sulfate (SDS) have been shown to exhibit a higher value of σ_{SF} and a lower surface tension than the pure liquid [60]. Also, the values of σ_{SF} and σ_{FG} change with temperature. The interfacial tension of water-air changes linearly with temperature with a sensitivity of -0.16 mN m^{-1} K^{-1} within the temperature range of 15 to 50°C [61]. The surface tension of the TWEEN®20 and SDS surfactants in water has also been shown to decrease linearly with temperature with a sensitivity independent of the surfactant concentration and in the same range as for distilled water [62]. Also, the interfacial tension of water-air changes linearly due to these surfactants with a sensitivity of -0.01 mg L^{-1} mN m^{-1} within temperature range of 5 to 50°C.

During the evaporation of colloidal suspension with surfactants, the internal flow changes the initial homogeneity of the suspension by carrying the solute and surfactants toward the contact line. By changing the concentration of the surfactants near the contact line, the surface tension at the contact line changes. This changes the balance of the interfacial forces at the contact line during the evaporation.

The effect of the temperature and surfactant concentration gradients on producing a Marangoni flow has been discussed previously. Hu and Larson showed that this effect suppresses the outward flow for droplets with a fully pinned contact line

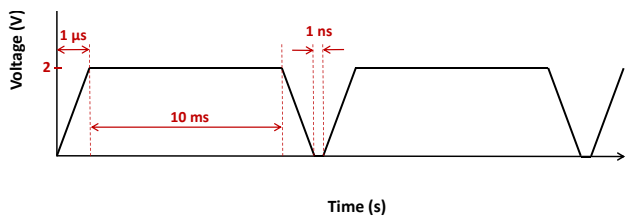

Figure 6.2: Signal properties of the micro dispenser unit. The tip of the nozzle was 1 mm above the substrate and we used 50 cycles to achieve a droplet with the diameter of 250 µm.

during the whole time of evaporation [27, 31]. While this assumption is useful for studying the Marangoni flow for a pinned droplet, in general it does not apply to the entire evaporation process. Here we study the effect of colloid and surfactant concentration on the contact line behavior during evaporation. We also show the effect of the substrate temperature on the evaporation stages and eventually discuss the effect of substrate temperature on the width of the deposit near the contact line.

6.2 Materials

Distilled water was used to prepare the suspensions with two different solid microsphere types: Fluoro-Max polystyrene beades (Bangs Laboratories, Inc., IN 46038, United States) with a diameter of 1 µm (S1) and surfactant-free white carboxyl/sulfate-fictionalized polystyrene beads (Life Technologies Inc., Burlington, ON, Canada) with a size of 0.6 µm (S2). We used TWEEN®20 as surfactant at different concentrations well below its critical micelle concentration ($C_{critical} \sim 0.01$ wt%). The concentration of solid microspheres of S1 and S2 and the concentration of surfactants in the colloidal suspension are C_{s1}, C_{s2} and C_{sur}, respectively. The printing setup was described in Section 3.2. The dispensing nozzle was actuated with the signal described in Figure 6.2. A Peltier device was used under the substrate (polystyrene coated plastic slide from Ted Pella Inc., CA 96049-2477, United States) to set the temperature and closed-loop control was used to maintain a constant temperature (details in Section 3.2.2).

6.3 Results and discussion

We investigate the contact line behavior of the droplets with particles and surfactant during evaporation in two different studies. We first study the effect of the surfactant and particles concentration on the pinned stage and the de-pinned stage of the droplet during evaporation at room temperature in Section 6.3.1. Then we show the effect of the substrate temperature on the contact line behavior of these droplets during the evaporation in Section 6.3.2. We study this effect when the substrate temperature is cooled below the ambient temperature. We also discuss the effect of the substrate temperature on the deposition of the particle ring after drying of the droplets with particles and surfactant.

By assuming an ideal three phase system, i.e. the solid surface is homogeneous and smooth, we can neglect the effect of the initial droplet size, R_0, on the receding contact line and the contact angle [56, 63–65]. Under these conditions and by neglecting the thermal and surfactant induced Marangoni effects, the behavior of the contact line represented by the normalized radius versus normalized time can be well scaled for all droplet sizes if we assume a negligible variation of the surface tension with the size of the droplet [56]. Therefore, to show the effect of colloids and surfactant concentration, we consider the normalized radius of the droplet $r(t)/R_0$ for an initial radius of $R_0 = 250$ µm for all droplets as a function of the evaporation time, normalized with the time over the total evaporation duration t/t_f.

Each data series represents the average of roughly 20 experiments that were conducted under the same conditions with a relative standard deviation of less than 1%. The minimum contact angle measurable by our imaging device is 8° and the data points with lower contact angles are not shown. At low concentration of the colloid particles (below 1%) and surfactants (below 0.05%) no major change in the initial contact angle of the droplets is observed (with an error less than 0.1%). Therefore, the total evaporation time, t_f for the droplets at low concentrations colloids and surfactants is the same and equal to 60 s (with 1% error).

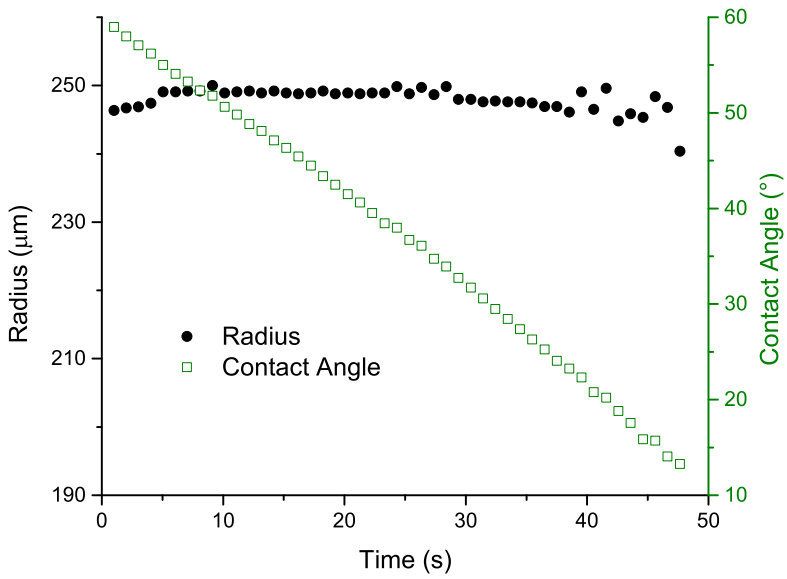

Figure 6.3: Measured radius and contact angle of a sessile droplet of a colloidal suspension containing S1 and surfactant at concentrations of 0.05 wt% and 0.0005 wt%, respectively, during evaporation at T = 24 °C.

6.3.1 Effect of surfactant and particle concentration on the contact line behavior

The effect of the solute particles and surfactant on the contact line during evaporation is assessed by measuring the radius and the contact angle of the droplet over time. As an example, Figure 6.3 shows the radius and the contact angle of a droplet containing S1 with the concentration C_{s1} = 0.05 wt% and surfactant with the concentration C_{sur} = 0.0005 wt%. The contact line of this droplet is pinned during the entire evaporation process, indicated by the constant droplet radius and the constantly decreasing contact angle.

The effect of the concentration of S2 on the behavior of the contact line is shown in Figure 6.4 with the normalized radius of the droplet with respect to the normalized time at different concentration of S2 from 0.014 to 0.8 wt%. The fluid was surfactant free and the liquid droplets evaporated at room temperature. No major change in the behavior of the contact line is observed at this range of concentrations that agrees with the results obtained by Okubo et al. [59]. To show the effect of sur-

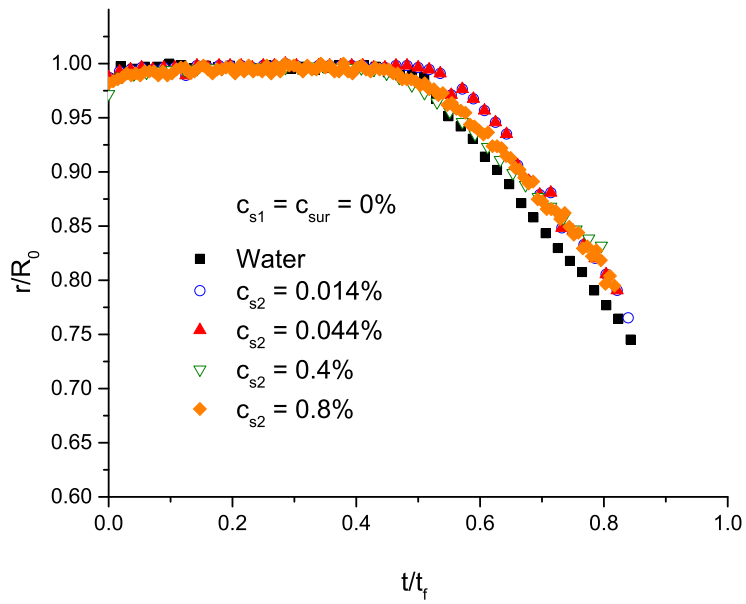

Figure 6.4: The effect of the concentration of S2 on the evaporation stages.

factant on the contact line and the contact angle behavior, solutions with different concentrations of surfactant up to 0.0005% were prepared. Figure 6.5 shows the normalized radius versus normalized time of these droplets. The evaporation starts with a pinned stage when the normalized radius of the droplet is equal to 1. After roughly half of the evaporation time passes (i.e. $t/t_f \cong 0.5$), the contact line starts to move and the normalized radius is reduced for low surfactant concentrations. At surfactant concentrations above 0.0002% the contact line stays fully pinned.

However, while increasing the surfactant concentration lengthens the duration of the pinned-stage of the droplet and pins its contact line fully, at concentrations near c_{sur} = 0.002 wt% and above, the surfactant significantly affects the initial droplet geometry. The initial contact angle of the droplet decreases by about 10° when the concentration of the surfactant is increased from 0.0005 wt% to 0.001 wt% as shown in Figure 6.6.

The effect of a combination of particles and surfactant on the contact line of the sessile droplets evaporating at room temperature is shown in Figure 6.7. The trend

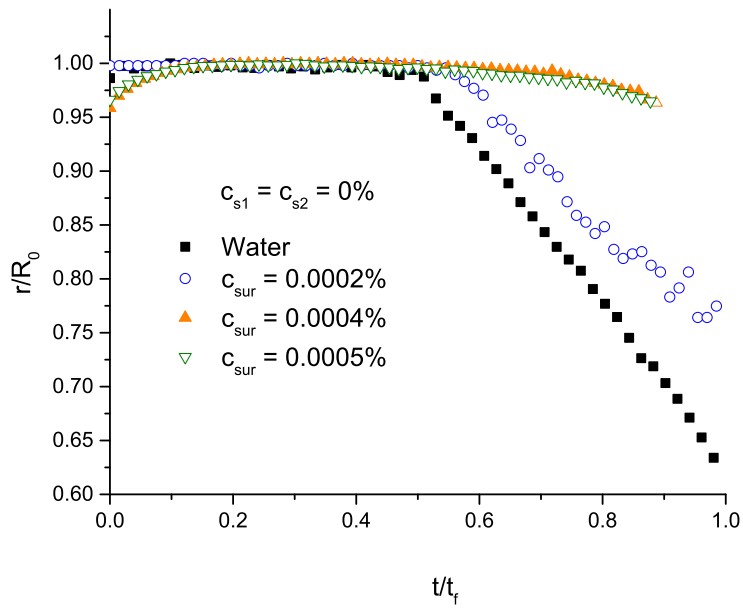

Figure 6.5: The effect of low concentrations of surfactant on the behavior of the contact line.

observed is similar to the effect of surfactant alone shown in Figure 6.5, and the particles do not seem to affect the contact line behavior as in Figure 6.6. The experiments suggest that the presence of solute solid microspheres of different sizes (S1 and S2) at concentrations up to 0.05% for S1 and 0.8% for S2 has no major effect on the behavior of the contact line (Figures 6.7 and 6.4, respectively), while the presence of surfactants increases the duration of the pinned stage during evaporation. This can be easily understood by impact of the presence of these solutes on the interfacial tensions. While low concentrations of microspheres do not change the surface tension, adding surfactant reduces it. This means that the surfactant reduces the surface tension as the main driving force for de-pinning, and thus the contact line stays pinned for a longer period during evaporation.

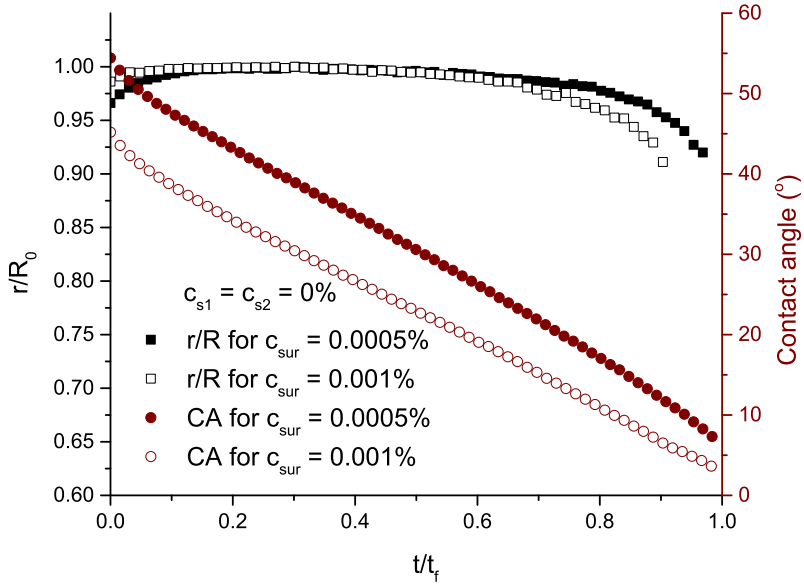

Figure 6.6: Normalized radius and contact angle measurement of the mixtures with higher amount of surfactants.

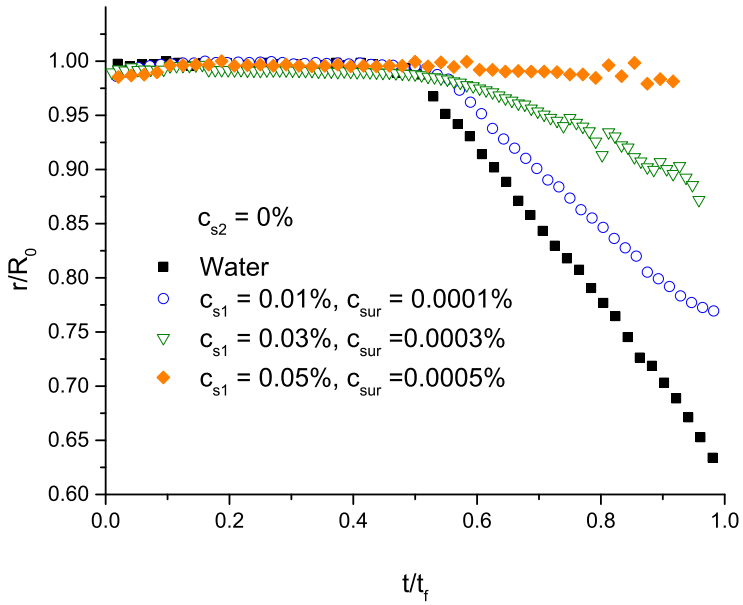

Figure 6.7: The effect of the concentration of S1 on evaporation stages.

6.3.2 Effect of substrate temperature on the contact line behavior and particle deposition

The effect of the substrate temperature on the contact line behavior is shown for solutions without and with surfactant and particles (S1) in Figure 6.8, at an ambient temperature of 24 °C and relative humidity of 49.3%. The total evaporation time is longer at lower substrate temperatures. The normalized radius of the droplet versus the normalized time during evaporation of water droplets at different temperatures is shown in Figure 6.8a. The same parameters are shown for the droplets with surfactant and particles (S1) in Figure 6.8b; according to the previous section we assume that the contact line behavior is affected by the surfactant alone and not by the particles. Particle deposition can therefore be studied without the particles affecting the internal flow inside droplets. For pure water, the temperature has a negligible effect on the evaporation modes as shown in Figure 6.8a. This is mainly due to the low sensitivity of the surface tension to temperature for water, and the thermal gradient across the droplet does not significantly affect the behavior of the contact line. When surfactant is added to the droplets, we observe no major change in the duration of the fully pinned stage at lower substrate temperature. However, at lower substrate temperature the de-pinned stage leads to a smaller final droplet radius as shown in Figure 6.8b. This is mainly because of the surface tension, that is the main force of de-pinning, is higher near the contact line when the substrate temperature is lower [62].

Figure 6.9 shows the deposition of particles (S1) near the contact line as a result of evaporation of droplets in Figure 6.8b. The particles deposit in one single layer on the substrate. We measured the width of the particle ring for droplet suspensions with 0.05 wt% S1 and 0.0005 wt% surfactant, δ at different substrate temperatures. The normalized width of particle deposition δ/R after evaporation as a function of substrate temperature is shown in Figure 6.10.

The effect of a lower substrate temperature on particle deposition at the contact line requires explanation. According to Figure 6.8b, the contact line stays pinned for the same normalized duration at all temperature. It will therefore stayed pinned for longer in absolute time at lower temperature. Therefore, the outward flow that carries particles to the contact line during evaporation persist for a longer amount of time. At the same time, the outward velocity magnitude is smaller for substrates

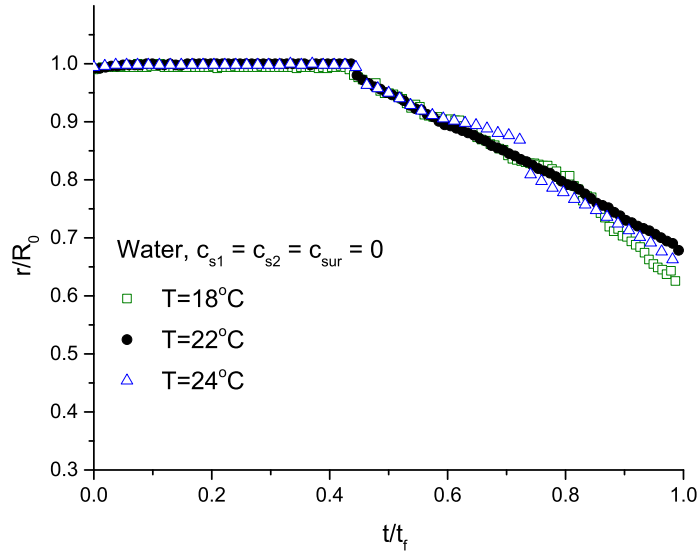

(a)

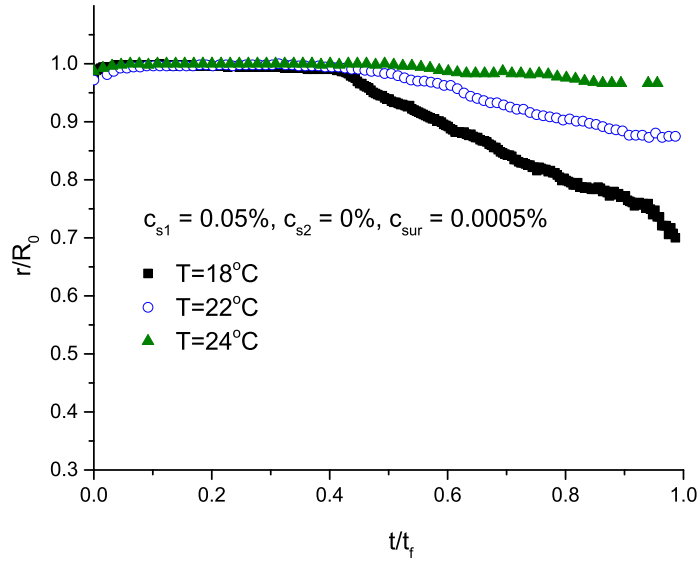

(b)

Figure 6.8: The effect of the substrate temperature on the behavior of the contact line for solutions (a) without and (b) with surfactant and particles.

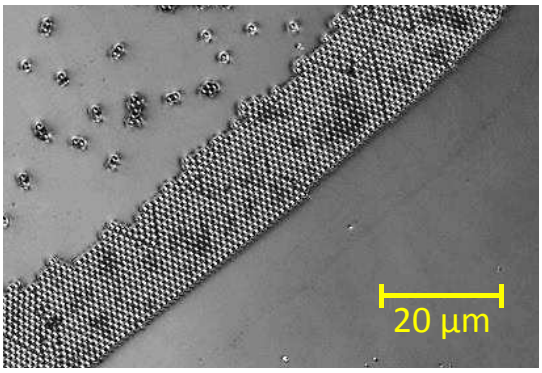

(a) T = 18°C

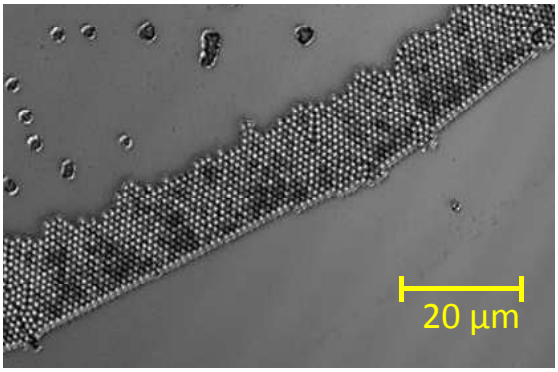

(b) T = 22°C

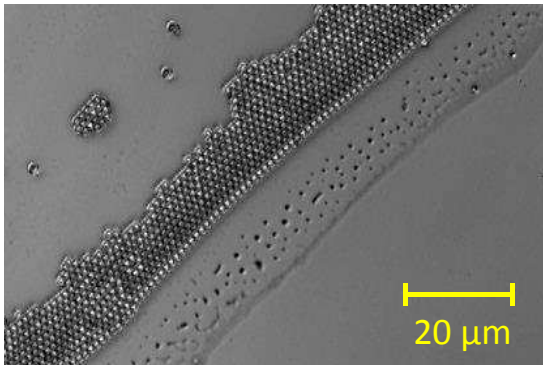

(c) T = 24°C

Figure 6.9: Particle deposition from a sessile droplet with 0.05% S1 and 0.0005% surfactant at different substrate temperatures. The initial radius of the droplets was $R_0 = 250$ µm.

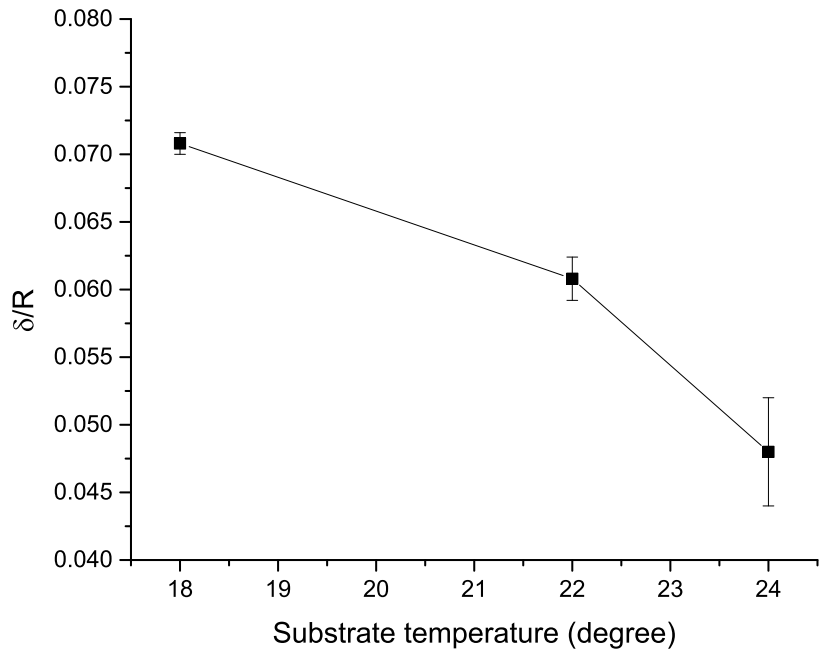

Figure 6.10: The normalized width of particle rings for droplets at different substrate temperature; the size of the error bars is the standard deviation of the average ring width for roughly 20 droplets with 0.05 wt% S1 and 0.0005 wt% surfactant for each temperature as shown partly in Figure 6.9.

at lower temperature due to the reduced evaporation rate. These two effects should cancel each other. However the particle ring has a larger width for sessile droplet suspensions at lower substrate temperature (Figure 6.9 and Figure 6.10).

The first apparent reason for a wider ring at lower temperature may seem to be the longer evaporation time and thus a longer pinned stage for the substrate at lower temperature. However, if we assume that all of the ring deposition happens at the pinned stage, we could see the total deposition

$$m_{\text{deposition}} \propto \left(\frac{dV}{dt}\right) t, \tag{6.2}$$

at time t where (dV/dt) is the evaporation rate. Approximating the evaporation rate with V/t_f, we see that the ring deposition is only a function of the normalized

time. This means that although the evaporation time for ring deposition is faster at lower temperatures, the average outward flow velocity is slower such that it leads to the same deposition mass. To explain the wide deposition band for lower temperature substrate, we need to account for the two types of flow for small droplets ($r < 1$ mm when gravity is negligible): viscous outward flow and Marangoni flow at the droplet surface.

For droplets with a pinned contact line, the evaporation-induced viscous flow toward the contact line keeps the substrate wet until the contact line by replacing the fluid that evaporates near the contact line. Hence, the viscous flow generated in a droplet with pinned contact line in the diffusion controlled evaporation is always outward [18, 19, 27]. However, the direction of the Marangoni flow at the surface of the droplet is somehow more complex. As mentioned earlier, for droplets with surfactant, the surface tension increases when the temperature decreases. When the substrate is at a lower temperature than the environment, the droplet surface is at its lowest temperature near the contact line. The surface tension is higher at a lower temperature and therefore a Marangoni flow is produced from the center toward the contact line at the surface of the droplet (Figure 6.11a). For evaporation at room temperature, the substrate temperature is not above the ambient temperature and evaporation would lower the temperature at the contact line. However, the temperature difference (ΔT) will be much smaller compared to the cooled substrate. It is worth pointing out that for a hot substrate at a temperature well above the ambient temperature, the Marangoni flow at the surface is in the opposite direction as shown in Figure 6.11b. This is due to the higher temperature near the contact line that leads to a lower surface tension, and generates a Marangoni flow at the surface toward the center of the droplet.

The magnitude of the Marangoni flow compared to the outward viscous flow can be compared using the dimensionless thermal Marangoni number

$$Ma = \frac{\beta \Delta T t_f}{\mu R}, \tag{6.3}$$

where β is the temperature sensitivity of the surface tension, ΔT is the temperature difference across the droplet and μ is the viscosity of the fluid. Deegan et al. [18] estimated that for a droplet evaporating at room temperature the amount of

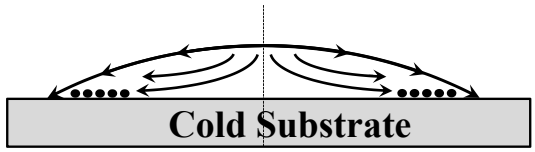

(a)

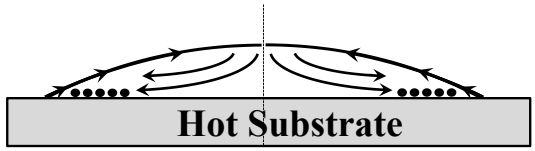

(b)

Figure 6.11: Evaporation induced flow for cold (a) and hot (b) substrates; Marangoni flow at the surface of the droplet carries the particles to the contact line with a cold substrate while it drives them away from the contact line with a hot substrate.

deposit carried by the Marangoni flow is around 10% of the total deposit. When the substrate temperature is reduced, the thermal Marangoni number is higher and the flow is stronger. Therefore more deposit is carried toward the contact line and leads to a ring deposition with a larger width (Figure 6.10).

6.4 Conclusions

The effect of colloids and surfactant on the evaporation of sessile water droplets was investigated. Microspheres of two different sizes (0.6 µm and 1 µm) were used to prepare suspensions at different concentrations, and the evaporation of droplets was studied at concentrations below 1%. No major change was observed in the behavior of the contact line and the contact line was almost pinned for near 50% of the whole evaporation time for all of the suspensions without surfactants. We also studied the effect TWEEN®20 as surfactant on the evaporation of sessile droplets. At low surfactant concentration below 0.0005 wt%, no major change in the ini-

tial contact angle and radius of the sessile droplets was observed. However, we observed an increase in the pinned-stage of the evaporation process and a lower receding contact angle. A fully pinned contact line was observed at surfactant concentration near 0.0005 wt%.

We also investigated the effect of the substrate temperature on the evaporation of distilled water and colloidal suspensions with a surfactant concentration of 0.0005 wt%. We measured the size of the ring deposition of microspheres after drying of colloidal suspensions with the surfactant concentration of 0.0005 wt% and we showed a wider ring at lower substrate temperature. We showed that the main reason that causes the wider ring deposition is a result of a stronger thermal Marangoni flow toward the contact line.

Chapter 7

Conclusions and future work

7.1 Conclusions

The basic evaporation models of sessile droplets on a flat substrate was discussed and the limitation of the models to predict the evaporation of small sessile droplets was discussed. The influence of the substrate thermal properties was confirmed through sets of experiments of water droplets evaporation on different substrates with different thermal conductivities. While the basic models predict that the evaporation rate per unit length of the droplet, i.e. $\left(\mathrm{d}V/\mathrm{d}t\right)/R$, yields the same value, the model predictions are from the experimental results. A numerical model was developed to include the thermal effects of the substrate. The numerical model confirmed that for thin droplets, substrate cooling has a strong influence on droplet evaporation rate and time. Furthermore, when the substrate is considered non-conductive, the results from our model approach the basic model. A dimensionless number was suggested that relates the influence of thermal properties on the evaporation process to the droplet size.

Furthermore, a model was developed for the evaporation of line droplets with finite aspect ratio. The complex behavior of the contact line in line droplets and the existence of both pinned and de-pinned stages simultaneously was discussed through a model that solves the most stable shape of the droplet during evaporation using energy equations. This approach de-coupled the evaporation equations from the energy equations. The evaporation flux was found by solving a Laplace equa-

tion in a quasi-steady state for diffusion-controlled evaporation. By knowing the evaporation flux and the geometrical shape of the most stable form of the droplet, the behavior of the contact line at the ends and at the sides was presented. Three different stages for the contact line were distinguished: fully pinned, de-pinned ends and pinned sides, fully de-pinned. Also, the model shows that total evaporation along the line droplet per unit area is higher near the ends. By having the shape of the droplet found using our model, the evaporation-induced flow inside line droplets was investigated inside line droplets. A potential flow assumption was used to find the velocity field. The outward evaporation-induced flow was shown inside the line droplets during evaporation.

Finally, the effect of surfactant and particles on the contact line behavior was discussed. Sets of experiments were run for colloidal suspensions containing different particles (of 0.6 μm and 1 μm) at different concentrations. No major effect on the behavior of the contact line was observed due to the presence of these particles at different concentrations. However, the surfactant concentration showed to have a major effect on the pinned an de-pinned stages during evaporation. At lower concentration of surfactant, below 0.0005 wt%, the duration of the pinned stage increased with increasing surfactant concentration. This was mainly due to the lower surface tension that is the main force for moving the contact line. The effect of the substrate temperature was also investigated. The cooling of the substrate showed no effect on the ratio of pinned and de-pinned stage at the absence of surfactant. At the presence of surfactant, cooling the substrate increased the ratio of the duration of the de-pinned to pinned stage. However, despite the longer duration of the de-pinned stage, a larger ring deposition was observed at lower temperature of the substrate. This was due to the Maranoni flow at the surface that carries the particle at the surface toward the contact line.

The major contributions of this thesis are:

- Developing a numerical model for the evaporation of sessile droplets that includes the effect of the substrate conductivity based on FLOW-3D subroutines

- Showing the strong influence of substrate thermal conductivity on evaporation of small droplets and finding a critical radius of droplets below which the substrate conductivity becomes substantial.
- Developing a new model based using an energy method to study the evaporation of line droplets where pinned and de-pinned segments of the contact line exist simultaneously
- Finding the outward evaporation-induced flow inside line droplets using a potential flow assumption
- Showing the effect of surfactants and particles on the pinned and de-pinned stages during the evaporation of sessile droplets of colloidal suspensions
- Investigating the effect of temperature on the pinned and de-pinned stages during the evaporation of sessile droplets of colloidal suspensions
- Studying the effect of temperature on the deposition of particles from sessile droplets of colloidal suspensions and showing the strong influence of the Maranoni flow at the surface on the deposition.

7.2 Future work

In evaporation of small droplet, the technique that was used in the numerical approach to include the thermal effects was to assume a uniform yet separate phase for air as a void. Although this is a better approximation than assuming a uniform temperature across the fluid-gas interface, the temperature discontinuity at the interface is not physically realistic. Also, the values of the vapor concentration and the diffusion coefficient change with the temperature gradient across the droplet. While for small droplets, the temperature difference is small and this gradient does not produce significant error, this effect should be included for larger droplets. As a future task, this error can be fixed by using the two fluid model with phase change and a non-condensable gas. This allows the saturation properties in a cell to be a function of the local vapor concentration, which is affected by both phase change and diffusion. However, this requires a new method for fixing the contact line during the pinned stage. The technique that was used here to fix the contact line by

defining a dummy substance in the void will no longer work. Also, since we used a fixed mesh, it is relatively easy to extend the numerical model to the droplet with different shapes, including line droplets and compare the results with the results presented here.

In evaporation of line droplets, a future step is to solve Stokes flow and Navier-Stokes and to compare the velocity fields from these flows with the potential flow. However, defining the slip velocity where both moving contact line and pinned contact line (no-slip) exist simultaneously will remain a challenge.

Bibliography

[1] R. G. Picknett and R. Bexon, "The evaporation of sessile or pendant drops in still air," *Journal of Colloid and Interface Science*, vol. 61, pp. 336–350, Sept. 1977. → pages viii, 8, 9, 18, 42

[2] H. Y. Erbil, "Evaporation of pure liquid sessile and spherical suspended drops: A review," *Advances in Colloid and Interface Science*, vol. 170, pp. 67–86, Jan. 2012. → pages 1

[3] R. Sharma, C. Y. Lee, J. H. Choi, K. Chen, and M. S. Strano, "Nanometer positioning, parallel alignment, and placement of single anisotropic nanoparticles using hydrodynamic forces in cylindrical droplets," *Nano Lett.*, vol. 7, no. 9, pp. 2693–2700, 2007. → pages 1, 54, 71

[4] S. Tokonami, H. Shiigi, and T. Nagaoka, "Review: Micro- and nanosized molecularly imprinted polymers for high-throughput analytical applications," *Analytica Chimica Acta*, vol. 641, pp. 7–13, May 2009. → pages 71

[5] A. A. Sagade and R. Sharma, "Copper sulphide (CuxS) as an ammonia gas sensor working at room temperature," *Sensors and Actuators B: Chemical*, vol. 133, pp. 135–143, July 2008. → pages

[6] W. R. Small, C. D. Walton, J. Loos, and M. in het Panhuis, "Carbon nanotube network formation from evaporating sessile drops," *The Journal of Physical Chemistry B*, vol. 110, pp. 13029–13036, July 2006. → pages 71

[7] S. H. Ko, H. Lee, and K. H. Kang, "Hydrodynamic flows in electrowetting," *Langmuir*, vol. 24, pp. 1094–1101, Feb. 2008. → pages 42

[8] T. T. Nellimoottil, P. N. Rao, S. S. Ghosh, and A. Chattopadhyay, "Evaporation-induced patterns from droplets containing motile and nonmotile bacteria," *Langmuir*, vol. 23, pp. 8655–8658, Aug. 2007. → pages 1

[9] R. Sharma and M. S. Strano, "Centerline placement and alignment of anisotropic nanotubes in high aspect ratio cylindrical droplets of nanometer diameter," *Advanced Materials*, vol. 21, no. 1, p. 6065, 2009. → pages 1, 54, 71

[10] V. Dugas, J. Broutin, and E. Souteyrand, "Droplet evaporation study applied to DNA chip manufacturing," *Langmuir*, vol. 21, pp. 9130–9136, Sept. 2005. → pages 2, 71

[11] Y.-C. Hu, Q. Zhou, Y.-F. Wang, Y.-Y. Song, and L.-S. Cui, "Formation mechanism of micro-flows in aqueous poly(ethylene oxide) droplets on a substrate at different temperatures," *Petroleum Science*, vol. 10, pp. 262–268, June 2013. → pages 2, 34, 54

[12] T.-S. Wong, T.-H. Chen, X. Shen, and C.-M. Ho, "Nanochromatography driven by the coffee ring effect," *Analytical Chemistry*, vol. 83, pp. 1871–1873, Mar. 2011. → pages 71

[13] J.-H. Kim, S.-B. Park, J. H. Kim, and W.-C. Zin, "Polymer transports inside evaporating water droplets at various substrate temperatures," *The Journal of Physical Chemistry C*, vol. 115, pp. 15375–15383, Aug. 2011. → pages 54

[14] S. Choi, S. Stassi, A. P. Pisano, and T. I. Zohdi, "Coffee-ring effect-based three dimensional patterning of Micro/Nanoparticle assembly with a single droplet," *Langmuir*, vol. 26, pp. 11690–11698, July 2010. → pages

[15] D. Wang, S. Liu, B. J. Trummer, C. Deng, and A. Wang, "Carbohydrate microarrays for the recognition of cross-reactive molecular markers of microbes and host cells," *Nature biotechnology*, vol. 20, pp. 275–281, Mar. 2002. PMID: 11875429. → pages 2, 54, 71

[16] H. K. Cammenga, "Evaporation mechanisms of liquids," *Current topics in materials science*, vol. 5, pp. 335–446, 1980. → pages 3

[17] C. Snow, "Potential problems and capacitance for a conductor bounded by two intersecting spheres," *Journal of Research of the National Bureau of Standards*, vol. 43, p. 337, 1949. → pages 9

[18] R. D. Deegan, O. Bakajin, T. F. Dupont, G. Huber, S. R. Nagel, and T. A. Witten, "Contact line deposits in an evaporating drop," *Physical Review E*, vol. 62, p. 756, July 2000. → pages 10, 14, 18, 27, 53, 54, 71, 84

[19] H. Hu and R. G. Larson, "Evaporation of a sessile droplet on a substrate," *The Journal of Physical Chemistry B*, vol. 106, pp. 1334–1344, Feb. 2002. → pages 12, 18, 29, 43, 44, 48, 49, 53, 61, 71, 84

[20] Y. O. Popov, "Evaporative deposition patterns: Spatial dimensions of the deposit," *Physical Review E*, vol. 71, p. 036313, Mar. 2005. → pages 14, 27, 43, 44, 45, 54

[21] H. Gelderblom, A. G. Marin, H. Nair, A. van Houselt, L. Lefferts, J. H. Snoeijer, and D. Lohse, "How water droplets evaporate on a superhydrophobic substrate," *Physical Review E*, vol. 83, no. 2, p. 026306, 2011. → pages

[22] F. Girard, M. Antoni, S. Faure, and A. Steinchen, "Influence of heating temperature and relative humidity in the evaporation of pinned droplets," *Colloids and Surfaces A: Physicochemical and Engineering Aspects*, vol. 323, pp. 36–49, June 2008. → pages 18

[23] Y. Y. Tarasevich, "Simple analytical model of capillary flow in an evaporating sessile drop," *Physical Review E*, vol. 71, p. 027301, Feb. 2005. → pages 19, 54, 62, 72

[24] A. J. Petsi and V. N. Burganos, "Potential flow inside an evaporating cylindrical line," *Physical Review E*, vol. 72, p. 047301, Oct. 2005. → pages 22, 55, 62, 68, 71

[25] A. J. Petsi and V. N. Burganos, "Evaporation-induced flow in an inviscid liquid line at any contact angle," *Physical Review E*, vol. 73, p. 041201, Apr. 2006. → pages 23, 53, 55, 72

[26] H. Masoud and J. D. Felske, "Analytical solution for stokes flow inside an evaporating sessile drop: Spherical and cylindrical cap shapes," *Physics of Fluids*, vol. 21, pp. 042102–042102–11, Apr. 2009. → pages 23, 55, 62, 71, 72

[27] H. Hu and R. G. Larson, "Analysis of the effects of marangoni stresses on the microflow in an evaporating sessile droplet," *Langmuir*, vol. 21, pp. 3972–3980, Apr. 2005. → pages 24, 28, 53, 54, 56, 62, 68, 71, 72, 74, 84

[28] R. Bhardwaj, X. Fang, and D. Attinger, "Pattern formation during the evaporation of a colloidal nanoliter drop: a numerical and experimental study," *New Journal of Physics*, vol. 11, p. 075020, July 2009. → pages 28

[29] A. Petsi, A. Kalarakis, and V. Burganos, "Deposition of brownian particles during evaporation of two-dimensional sessile droplets," *Chemical Engineering Science*, vol. 65, pp. 2978–2989, May 2010. → pages 28

[30] J. Park and J. Moon, "Control of colloidal particle deposit patterns within picoliter droplets ejected by ink-jet printing," *Langmuir*, vol. 22, pp. 3506–3513, Apr. 2006. → pages 28

[31] H. Hu and R. G. Larson, "Marangoni effect reverses coffee-ring depositions," *The Journal of Physical Chemistry B*, vol. 110, pp. 7090–7094, Apr. 2006. → pages 29, 74

[32] K. H. Kang, S. J. Lee, C. M. Lee, and I. S. Kang, "Quantitative visualization of flow inside an evaporating droplet using the ray tracing method," *Measurement Science and Technology*, vol. 15, pp. 1104–1112, June 2004. → pages 34

[33] S. T. Beyer and K. Walus, "Controlled orientation and alignment in films of single-walled carbon nanotubes using inkjet printing," *Langmuir*, vol. 28, pp. 8753–8759, June 2012. → pages 42, 71

[34] G. McHale, "Surface free energy and microarray deposition technology," *Analyst*, vol. 132, pp. 192–195, Feb. 2007. → pages 42

[35] R. Bhardwaj, X. Fang, P. Somasundaran, and D. Attinger, "Self-assembly of colloidal particles from evaporating droplets: Role of DLVO interactions and proposition of a phase diagram," *Langmuir*, vol. 26, pp. 7833–7842, June 2010. → pages 42

[36] G. J. Dunn, S. K. Wilson, B. R. Duffy, S. David, and K. Sefiane, "The strong influence of substrate conductivity on droplet evaporation," *Journal of Fluid Mechanics*, vol. 623, no. 1, p. 329351, 2009. → pages 44

[37] M. S. Plesset and A. Prosperetti, "Flow of vapour in a liquid enclosure," *Journal of Fluid Mechanics*, vol. 78, pp. 433–444, 1976. → pages 44

[38] S. Das, P. R. Waghmare, M. Fan, N. S. K. Gunda, S. S. Roy, and S. K. Mitra, "Dynamics of liquid droplets in an evaporating drop: liquid droplet coffee stain? effect," *RSC Advances*, vol. 2, pp. 8390–8401, Aug. 2012. → pages 53

[39] B. J. Fischer, "Particle convection in an evaporating colloidal droplet," *Langmuir*, vol. 18, pp. 60–67, Jan. 2002. → pages 54

[40] J. L. Wilbur, A. Kumar, H. A. Biebuyck, E. Kim, and G. M. Whitesides, "Microcontact printing of self-assembled monolayers: applications in microfabrication," *Nanotechnology*, vol. 7, p. 452, Dec. 1996. → pages 54

[41] T. Kawase, H. Sirringhaus, R. H. Friend, and T. Shimoda, "Inkjet printed via-hole interconnections and resistors for all-polymer transistor circuits," *Advanced Materials*, vol. 13, no. 21, p. 16011605, 2001. → pages 71

[42] B.-J. de Gans, P. C. Duineveld, and U. S. Schubert, "Inkjet printing of polymers: State of the art and future developments," *Advanced Materials*, vol. 16, no. 3, p. 203213, 2004. → pages 71

[43] H. Sirringhaus, T. Kawase, R. H. Friend, T. Shimoda, M. Inbasekaran, W. Wu, and E. P. Woo, "High-resolution inkjet printing of all-polymer transistor circuits," *Science*, vol. 290, pp. 2123–2126, Dec. 2000. PMID: 11118142. → pages

[44] D. Soltman and V. Subramanian, "Inkjet-printed line morphologies and temperature control of the coffee ring effect," *Langmuir*, vol. 24, pp. 2224–2231, Mar. 2008. → pages 54

[45] R. Tadmor and P. S. Yadav, "As-placed contact angles for sessile drops," *Journal of Colloid and Interface Science*, vol. 317, pp. 241–246, Jan. 2008. → pages 56

[46] J. Drelich, "The significance and magnitude of the line tension in three-phase (solid-liquid-fluid) systems," *Colloids and Surfaces A: Physicochemical and Engineering Aspects*, vol. 116, pp. 43–54, Sept. 1996. → pages 56

[47] R. Tadmor, "Line energy, line tension and drop size," *Surface Science*, vol. 602, pp. L108–L111, July 2008. → pages 69

[48] C.-H. Choi and C.-J. C. Kim, "Droplet evaporation of pure water and protein solution on nanostructured superhydrophobic surfaces of varying heights," *Langmuir*, vol. 25, pp. 7561–7567, July 2009. → pages 71

[49] K. F. Baughman, R. M. Maier, T. A. Norris, B. M. Beam, A. Mudalige, J. E. Pemberton, and J. E. Curry, "Evaporative deposition patterns of bacteria from a sessile drop: Effect of changes in surface wettability due to exposure to a laboratory atmosphere," *Langmuir*, vol. 26, pp. 7293–7298, May 2010. → pages

[50] D. Brutin, B. Sobac, and C. Nicloux, "Influence of substrate nature on the evaporation of a sessile drop of blood," *Journal of Heat Transfer*, vol. 134, pp. 061101–061101, May 2012. → pages 71

[51] D. Pech, M. Brunet, P.-L. Taberna, P. Simon, N. Fabre, F. Mesnilgrente, V. Condra, and H. Durou, "Elaboration of a microstructured inkjet-printed carbon electrochemical capacitor," *Journal of Power Sources*, vol. 195, pp. 1266–1269, Feb. 2010. → pages 71

[52] J. Bachmann, A. Ellies, and K. Hartge, "Development and application of a new sessile drop contact angle method to assess soil water repellency," *Journal of Hydrology*, vol. 231232, pp. 66–75, May 2000. → pages 71

[53] H. Y. Erbil, G. McHale, and M. I. Newton, "Drop evaporation on solid surfaces: constant contact angle mode," *Langmuir*, vol. 18, no. 7, pp. 2636–2641, 2002. → pages

[54] X. Fang, B. Li, J. C. Sokolov, M. H. Rafailovich, and D. Gewaily, "Hildebrand solubility parameters measurement via sessile drops evaporation," *Applied Physics Letters*, vol. 87, pp. 094103–094103–3, Aug. 2005. → pages

[55] Y. C. Jung and B. Bhushan, "Wetting behaviour during evaporation and condensation of water microdroplets on superhydrophobic patterned surfaces," *Journal of Microscopy*, vol. 229, no. 1, p. 127140, 2008. → pages 71

[56] J. Drelich, J. D. Miller, and R. J. Good, "The effect of drop (bubble) size on advancing and receding contact angles for heterogeneous and rough solid surfaces as observed with sessile-drop and captive-bubble techniques," *Journal of Colloid and Interface Science*, vol. 179, pp. 37–50, Apr. 1996. → pages 72, 75

[57] D. Bargeman and F. Van Voorst Vader, "Effect of surfactants on contact angles at nonpolar solids," *Journal of Colloid and Interface Science*, vol. 42, pp. 467–472, Mar. 1973. → pages 73

[58] J. Menezes, J. Yan, and M. Sharma, "The mechanism of alteration of macroscopic contact angles by the adsorption of surfactants," *Colloids and Surfaces*, vol. 38, no. 2, pp. 365–390, 1989. → pages

[59] T. Okubo, "Surface tension of structured colloidal suspensions of polystyrene and silica spheres at the air-water interface," *Journal of Colloid and Interface Science*, vol. 171, pp. 55–62, Apr. 1995. → pages 73, 76

[60] R. Pyter, G. Zografi, and P. Mukerjee, "Wetting of solids by surface-active agents: The effects of unequal adsorption to vapor-liquid and solid-liquid interfaces," *Journal of Colloid and Interface Science*, vol. 89, pp. 144–153, Sept. 1982. → pages 73

[61] T. Mitsui, S. Nakamura, F. Harusawa, and Y. Machida, "Changes in the interfacial tension with temperature and their effects on the particle size and stability of emulsions," *Kolloid-Zeitschrift und Zeitschrift fr Polymere*, vol. 250, pp. 227–230, Mar. 1972. → pages 73

[62] S. Phongikaroon, R. Hoffmaster, K. P. Judd, G. B. Smith, and R. A. Handler, "Effect of temperature on the surface tension of soluble and insoluble surfactants of hydrodynamical importance," *Journal of Chemical & Engineering Data*, vol. 50, pp. 1602–1607, Sept. 2005. → pages 73, 80

[63] V. S. Vesselovsky and V. N. Pertzov, "Adhesion of air bubbles to the solid surface," *Zh. Fiz. Khim*, vol. 8, pp. 245–259, 1936. → pages 75

[64] Hideo Nakae, Ryuichi Inui, Yosuke Hirata, and Hiroyuki Saito, "Effects of surface roughness on wettability," *Acta Materialia*, vol. 46, pp. 2313–2318, Apr. 1998. → pages

[65] R. J. Good and M. Koo, "The effect of drop size on contact angle," *Journal of Colloid and Interface Science*, vol. 71, pp. 283–292, Sept. 1979. → pages 75

Appendix A

Geometrical calculations of the sessile droplets

A.1 Introduction

When a small sessile droplet is deposited on a substrate, it readily attains an equilibrium shape while there is a balance between interfacial forces acting on the droplet. As we discussed in Chapter 2 for small droplets, when the effect of gravity is negligible, the only forces acting on the droplets are Laplacian hydrostatic forces that make the spherical cap shape as the most stable form. Here we show the geometrical calculations of the spherical cap for point droplets that were used in the previous chapters.

A.2 Spherical cap calculations

For a point droplet with a circular footprint radius of R and the equilibrium contact angle of θ as shown in Figure A.1, we can find the radius of the spherical cap a as

$$a = \frac{R}{\sin\theta}. \tag{A.1}$$

If we write a based on h_m and R as:

$$a^2 = (a - h_m)^2 + R^2 \tag{A.2}$$

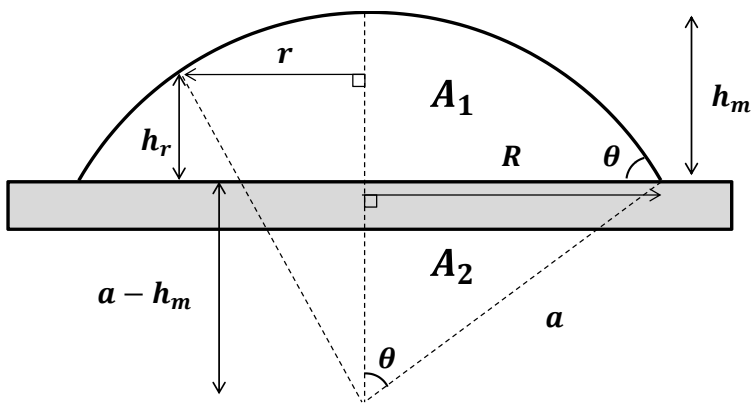

Figure A.1: Schematic of a sessile droplet on a substrate

then we will find

$$a = \frac{h_m^2 + R^2}{2h_m}. \tag{A.3}$$

We can also find θ in terms of R and h_m by rewriting Equation A.1 as:

$$\sin\theta = \frac{2Rh_m}{h_m^2 + R^2}, \tag{A.4}$$

or

$$\theta = \arcsin\left(\frac{2Rh_m}{h_m^2 + R^2}\right). \tag{A.5}$$

The height of the droplet, h_m, can be written in terms of a and θ as

$$a - h_m = a\cos\theta, \tag{A.6}$$

and thus:

$$h_m = a\left(1 - \cos\theta\right). \tag{A.7}$$

By replacing a from Equation A.1 into Equation A.7, we can write h_m in terms of R and θ as:

$$\begin{aligned} h_m &= \frac{R}{\sin\theta}(1-\cos\theta) \\ &= \frac{R}{\sin\theta}\left(1-1-2\sin^2\left(\frac{\theta}{2}\right)\right) \\ &= \frac{R}{2\sin\left(\frac{\theta}{2}\right)\cos\left(\frac{\theta}{2}\right)}\cdot 2\sin^2\left(\frac{\theta}{2}\right), \end{aligned} \tag{A.8}$$

to find

$$h_m = R\tan\left(\frac{\theta}{2}\right). \tag{A.9}$$

The cross sectional area of the droplet, A, can be calculated by subtracting the triangle area of $2A_2$ from a minor circular sector seen by 2θ as:

$$\begin{aligned} A &= \frac{2\theta}{2\pi}\pi a^2 - 2A_2 \\ &= \theta a^2 - 2\cdot\frac{1}{2}\cdot\frac{R}{\tan\theta}\cdot R \\ &= \frac{\theta R^2}{\sin^2\theta} - \frac{R^2}{\tan\theta} \end{aligned} \tag{A.10}$$

The volume of the droplet,V, can be found by calculating the volume of the spherical segment as:

$$\begin{aligned} V &= \int_0^{h_m} \pi r^2 \,\mathrm{d}h_r \\ &= \int_0^{h_m} 2\pi\left(a^2-(h_r+a-h_m)^2\right)\mathrm{d}h_r \\ &= \int_0^{h_m} \pi\left(2ah_m+2h_mh_r-2ah_r-h_r^2-h_m^2\right)\mathrm{d}h_r \\ &= \pi\left(2ah_mh_r+h_mh_r^2-ah_r^2-\frac{h_r^3}{3}-h_m^2h_r\right)\Bigg|_0^{h_m} \\ &= \frac{\pi}{3}h_m^2(3a-h_m). \end{aligned} \tag{A.11}$$

By inserting the Equation A.7 into Equation A.11, we can write the volume of the droplet as

$$\begin{aligned} V &= \frac{\pi}{3} a^2 (1-\cos\theta)^2 (3a - a(1-\cos\theta)) \\ &= \frac{\pi}{3} a^3 (1-\cos\theta)^2 (2+\cos\theta), \end{aligned} \tag{A.12}$$

or

$$\begin{aligned} V &= \frac{\pi}{3} \left(\frac{R}{\sin\theta}\right)^3 (1-\cos\theta)^2 (2+\cos\theta) \\ &= \frac{\pi R^3}{3\sin^3\theta} \left(\cos^3\theta - 3\cos\theta + 2\right). \end{aligned} \tag{A.13}$$

in terms of R and θ. Also, from Equation A.11 and Equation A.3, we can find the volume of the droplet as a function of R and h_m:

$$\begin{aligned} V &= \frac{\pi}{3} h_m (3ah_m - h_m) \\ &= \frac{\pi}{3} h_m \left(\frac{3}{2}\left(R^2 + h_m^2\right) - h_m^2\right) \\ &= \frac{\pi}{6} h_m \left(3R^2 + h_m^2\right). \end{aligned} \tag{A.14}$$

A.3 Sectional parameters across the droplet

The sectional area of the spherical cap is shown in Figure A.2. To find the section height h_r, we can write

$$a^2 = (a - h_m + h_r)^2 + r^2, \tag{A.15}$$

similar to Equation A.2 and find h_r as:

$$h_r = \sqrt{a^2 - r^2} - h_m - a, \tag{A.16}$$

or

$$h_r = \sqrt{\left(\frac{R}{\sin\theta}\right)^2 - r^2} - \frac{R}{\tan\left(\frac{\theta}{2}\right)} - \frac{R}{\sin\theta}, \tag{A.17}$$

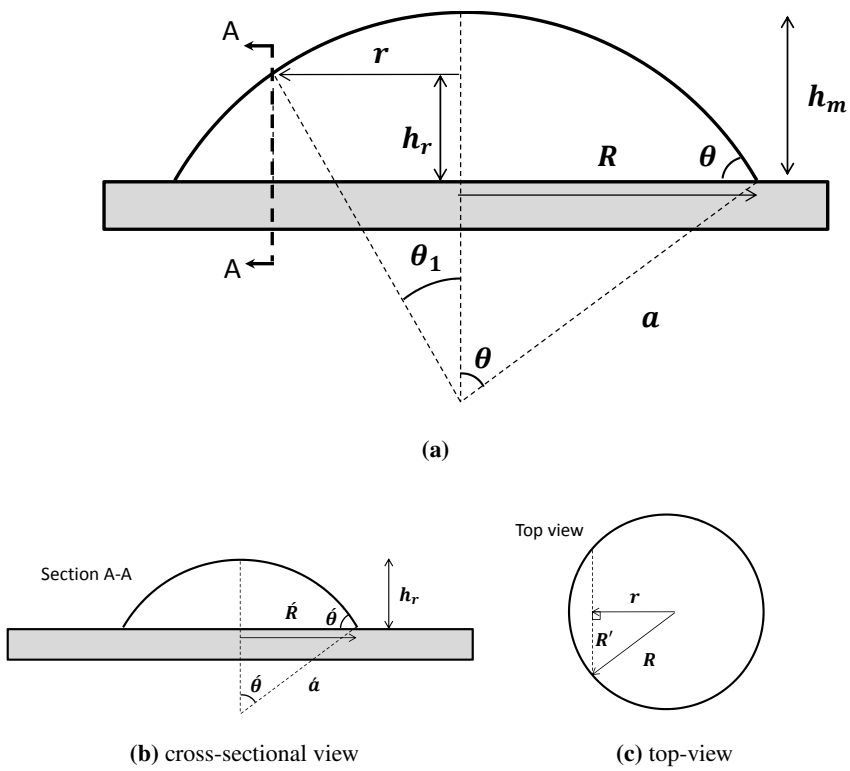

Figure A.2: Sectional parameters of a droplet in a sessile droplet.

in terms of R, θ and r. We can also write the section height in terms of θ_1 as:

$$h_r = \frac{r}{\tan(\theta_1)} + h_m - a, \tag{A.18}$$

where θ_1 is equal to

$$\theta_1 = \arcsin\left(\frac{r}{a}\right). \tag{A.19}$$

Finally we can find the sectional curvature of the droplet (Section A-A in Figure A.2b). The sectional area is the segment of a circle with the radius of R' that can be calculated versus R and r from Figure A.2c as:

$$R' = \sqrt{R^2 - r^2}. \tag{A.20}$$

Hence, we can find the sectional contact angle using the Equation A.8 as:

$$\begin{aligned}
\theta' &= 2\arctan\left(\frac{h_r}{R'}\right) \\
&= 2\arctan\left(\frac{h_m - a + \frac{r}{\tan(\theta_1)}}{\sqrt{R^2 - r^2}}\right) \\
&= 2\arctan\left(\frac{h_m - a + \frac{r}{\tan\left(\arcsin\left(\frac{r}{a}\right)\right)}}{\sqrt{R^2 - r^2}}\right). \qquad \text{(A.21)}
\end{aligned}$$

And eventually, we can find the radius of sectional curvature using Equation A.1 as:

$$\begin{aligned}
a' &= \frac{R'}{\sin\theta'} \\
&= \frac{R'}{\sin\left(2\arctan\left(\frac{h_m - a + \frac{r}{\tan\left(\arcsin\left(\frac{r}{a}\right)\right)}}{\sqrt{R^2 - r^2}}\right)\right)}. \qquad \text{(A.22)}
\end{aligned}$$